Chapter Six

Mr. Edwin Lai
Hong Kong Observatory

6. Tropical Cyclone Rainfall and Flood Forecasting

6.1 Introduction and basic hydrology

Tropical cyclones (TCs) are one of Mother Nature's most destructive forces. Coastal and island communities in the tropical and sub-tropical areas around the world are particularly vulnerable to their furies. Dangerous winds and storm surges can create significant damage to property and loss of lives. After landfall, TCs will begin to weaken due to lack of moisture and land interaction. Therefore, winds usually are not the primarily concern for inland communities farther away from the coast. Instead, torrential rains will be the major problem for inland areas along the path of the cyclone. Factors such as orographic lifting and interaction with cold fronts and other sub-tropical weather systems can further enhance the chance for locally heavy rainfall.

Forecasting flooding during the passage of a TC involves both meteorology and hydrology. The use of local radar, satellite imagery and mesoscale computer models can aid on predicting where the heavy rainfall will occur, and which areas will have the higher potential for flooding. Understanding the hydrological conditions of these areas beforehand can provide clues on the type, severity and duration of flooding.

Once rain has fallen on land, much of it will infiltrate into the soil and eventually become groundwater, being stored in aquifers. The rest of it will move across land as runoff to streams and rivers, which flow into larger bodies of surface water such as ponds, lakes and oceans at discharge points. Runoff includes water that flows on land surfaces known as surface runoff and also beneath the soil surface, called interflow. Since runoff is the main contributor of excessive water near the ground surface as well as into streams and rivers during a rain event, it is the most important component of flood forecasting.

6.1.1 Surface runoff

The amount of rain turning into surface runoff is determined by the characteristics of the surface or soil. Larger soil particles such as gravel and sand contain large pores which allow a higher infiltration rate. On the other hand, smaller soil particles such as silt and clay contain small pores which create a lower infiltration rate. However, smaller soil particles contain more pores in a given volume compared to larger soil particles. Therefore, the total void space in a given volume is higher in silt and clay than sand and gravel. This gives silt and clay a higher infiltration capacity, the ability to hold a larger volume of water.

During a short but heavy downpour, surface runoff will likely occur on top of soil with a high content of silt and clay. For a long period of moderate rain, surface runoff will start to accumulate on top of gravelly and sandy soil first. Human activity, including urbanization, deforestation and forest fires, can have an important effect on surface runoff as well. Concrete and asphalt surfaces commonly found in urban areas can create rapid surface runoff due to both low infiltration rate and low capacity. Deforestation and forest fires both drastically change the soil properties of affected areas, making them more subject to surface runoff than the surrounding unaffected areas.

6.1.2 Interflow

After being absorbed into the soil just beneath the surface, water tends to travel toward a lower elevation due to gravity. As a result, interflow will move from higher areas or ridges toward lower areas or valleys in a basin. Streams or tributaries can form along these local valleys as interflow from the surrounding high ground merges and continues to flow toward the bottom of the basin. Once it has reached the bottom of the basin, the accumulated water will become a river and keep surging into the lowest point of the basin, which is known as a discharge point.

Interflow tends to travel faster in soil with larger pores such as sand and gravel, while the opposite occurs in silt and clay with smaller pores. Pre-existing voids and tunnels created by both biological and human activity underneath the ground surface can greatly enhance interflow; this process is called transmissivity feedback. In areas where a shallow layer of soil is on top of bedrock, concrete or another layer of low-permeable soil such as compact clay, saturation will happen more quickly and horizontal water movement will also increase.

6.1.3 Basin properties

Basins have different sizes, shapes and characteristics, which contribute to various volumes and rates of runoff. For basins with identical size but different shapes, water will need to travel a longer distance from the highest to the lowest point in a long and narrow basin. Also, water entering the basin closer to the discharge point will arrive there sooner. This creates a more gradual increase in flow volume and a lower peak flow, as compared to round and wider basins. For basins that are similar in shape but different in size, the distance between the highest point and lowest point is much shorter for a small basin. On top of this, a rain storm will likely cover an entire small basin but only a portion of a large basin. As a result, flow volume will rise more rapidly and yield a higher peak flow in the smaller basin.

Gravity will cause water to move much faster in a steep basin than a flat one, resulting in a faster flow volume and higher peak flow as well. Basins with streams and tributaries that are either denser or less meandering or both will also produce a higher peak flow. Surface conditions of a stream or river can affect its runoff to the discharge point. A smooth stream or river bed will allow a more efficient runoff, while a rough bottom will hinder the movement of water and decrease its flow rate and volume.

6.1.4 Pre-event water

Except under extreme drought, a certain amount of water is always present in the soil above the aquifers. The amount depends on the frequency of rainfall and type of soil. Pre-event water is defined as water already existing in the soil and later being displaced into streams and rivers by interflow from newly fallen rain. After frequent rainstorms, most soil will become saturated or nearly saturated regardless of soil type. However, as mentioned earlier, soil with high silt and clay content can hold a higher volume of water. Therefore, streams and rivers with such soil properties will receive a higher amount of interflow during a rain event and rise faster and higher. When rain occurs infrequently, soil moisture content will be lower in gravelly and sandy soil with a higher infiltration rate, as most pre-existed water has infiltrated deeper into the aquifers below over time. This causes part of the new rainfall to be absorbed into the soil until saturation is reached. Only after this point will interflow begin to travel into the streams and rivers so that the rise is slower and not as high.

6.2 Types of flooding

The combination of the speed, intensity, and size of a tropical cyclone, along with soil properties, pre-existing moisture and local topography, will determine what kind of flooding will occur first and sequentially.

6.2.1 Flash flooding

Flash floods are rapidly occurring events. This type of flood can begin within a few minutes or hours of excessive rainfall. The rapidly rising water can reach heights of 30 feet or more and can roll boulders, rip trees from the ground, and destroy buildings, bridges and roads.

A fast moving intense cyclone with strong convection is likely to produce locally heavy downpours in its path. If a high amount of pre-event water is present in the soil, it will quickly be transferred into streams and rivers. Due to soil saturation, surface runoff will also form rapidly and add to the flow. Water levels in streams, rivers and storm drainage systems can rise very quickly to significant heights and overflow the banks, leading to flash floods. Since the amount of rainfall is limited by the fast speed of the cyclone, the flash flood will only last from several hours to a perhaps a day.

The worst case scenario is a large, slow-moving intense cyclone, bringing long lasting and widespread heavy rain. With saturated ground, flash floods will occur as described above but will then be followed by widespread inland flooding. Eventually, flash flooding streams and rivers will transform into long-term river flooding in large areas, but on relatively small islands, flood waters will reach the ocean in a matter of hours.

6.2.2 Area and inland flooding

Area and inland floods are also rapid events although not quite as rapid or locally severe as a flash flood. Still, streets can become swift-moving rivers and basements can become death traps as they fill with water. A primary cause is the conversion of fields or woodlands to roads and parking lots.

After short-term heavy rain events created by fast moving storms, area and inland floods are usually found in areas with low infiltration rates such as urban communities with concrete and asphalt, and rural communities with compact silt and clay. Nearly 100 percent of the rainfall will convert into surface runoff instantly and travel toward streams, rivers, storm drains and other low-lying areas. Minor to moderate flooding can then take place in low-lying areas as surface runoff collects. Once downpours have stopped, excessive surface runoff will diminish rapidly. However, it can still take several days to a few weeks for flooded low-lying areas to dry out.

For long periods of moderate to occasionally heavy rain caused by slow and weakening cyclones, area and inland floods will probably be found in low-lying areas with low infiltration materials and/or poor drainage. Surface runoff is expected to gradually accumulate in these areas and cause water levels to rise steadily. Once areas have become flooded, it might take several days for the water to drain out after the last measurable rain.

6.2.3 River flooding

River floods are longer term events and occur when the runoff from torrential rains, brought on by decaying tropical cyclones, reaches the rivers. A lot of the excessive water in river floods may begin as flash floods. River floods can occur in just a few hours and also last a week or longer. After pre-event water in the soil has been displaced into streams and rivers by newly-fallen rain, this infiltrated rain water will follow on its way to the same streams and rivers. For a small basin, it can take as little as a few hours to a day for this water to reach its destination. However, due to limited amounts of rain from the fast moving storm, and the lower quantity of rain water collected by the small basin, water levels tend to drop after a few days. For a large basin, water levels can remain at flood stage from several days to a week.

Instead of bursts of torrential rain, decaying storms with a slow pace will likely produce continuous moderate rain for several days. The potential for flash flooding is low but water levels in streams and rivers will steadily rise above flood levels and remain so for a few weeks. On the other hand, if the intensity of a storm is much stronger, rain may be heavy for several days. Under these circumstances, flash flooding will become long term flooding and can last for weeks.

The sizes of storms can also affect the severity of river flooding, mainly in large basins. A small storm over a large basin will create moderate flooding since only parts of the basin will be receiving rainfall. With a large storm, it is likely that most or the whole basin will be subject to rainfall, leading to more serious flooding. Regardless of storm sizes, small basins will likely receive near 100 percent rain coverage.

Small mountainous islands have both small basins and rivers/streams with relatively short distances to the discharge points, namely the ocean. On these islands, the main threat is the flash flood, which can occur rapidly as a TC approaches and end rapidly as it moves away. Very high rain rates can occur in the eyewall cloud of a TC. On Guam (an island of 212 sq mi/3139 sq km with an elevation of 1313 ft/400 m), during Typhoon Pongsona (December 2002), rain rates as high as 7.22 in/hr (183 mm/hr) were measured.

6.2.4 Mudslides and debris flows

Mudslides or debris flows kill thousands of people each year. Those initiated by tropical cyclones account for about 25 percent of all fatalities. Mudslides/debris flows occur in hilly or mountainous areas of saturated, low permeability soils such as clays, where relatively heavy rains continue after saturation is attained. The greatest chance of mudslides occurs where the slope of the face of a hill or mountain made of clay or similar material has an angle from the vertical of 10° to 40°. Here, gravity is most likely to overcome the chemical bonding of the water molecules that surround the clay molecules. The most likely areas for mudslides are: (1) clay areas where vegetation has been removed; clay areas where mudslides occurred before but bedrock is not yet exposed; steep clay areas at least 20 ft (6 m) high. The Weather Service Office on Guam has determined the critical elements needed for mudslides to occur on the high islands of Micronesia in the Northwest Pacific (see Table 6.1). The forecast requirements are also shown that enable the islands time to warn and evacuate the threatened populations (Table 6.1). Figure 6.1 shows (a) a model of the saturated clay molecule and (b) a diagram of the terrain slopes most vulnerable to mudslides.

Table 6.1. Critical parameters for mudslide occurrence in the mountain islands of Micronesia. Parameters for issuing warnings for mudslides in Micronesia. All islands have long-chain clay molecules except for Palau, which has short-chained clay molecules. Rainfall is in inches and millimeters.

	Long-Chain Clay Molecules (All High Islands but Palau)	**Short-Chain Clay Molecules (Palau only)**
Angle from Vertical	10°-40°	10°-40°
Rain Required for Slides	24-hr Rain 10 inches (254 mm)	24-hr Rain 7 inches (178 mm)

Rain Required for Slides	36-hr Rain 15 inches (381 mm)	36-hr Rain 10 inches (254 mm)
Rain Required for Warnings	24-hr Rain 7 inches (178 mm)	24-hr Rain 5 inches (127 mm)
Rain Required for Warnings	36-hr Rain 10 inches (254 mm)	36-hr Rain 7 inches (178 mm)

(a)

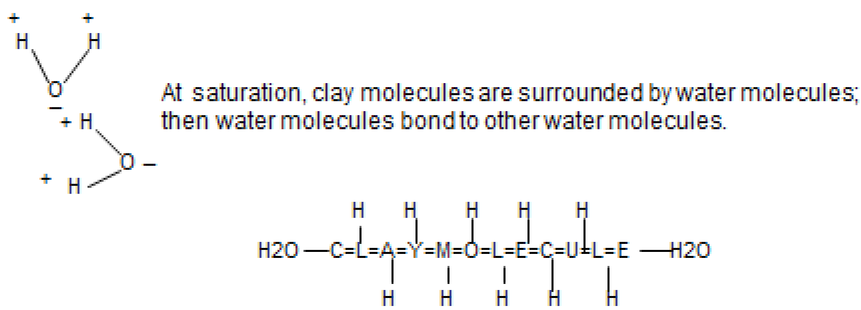

(b)

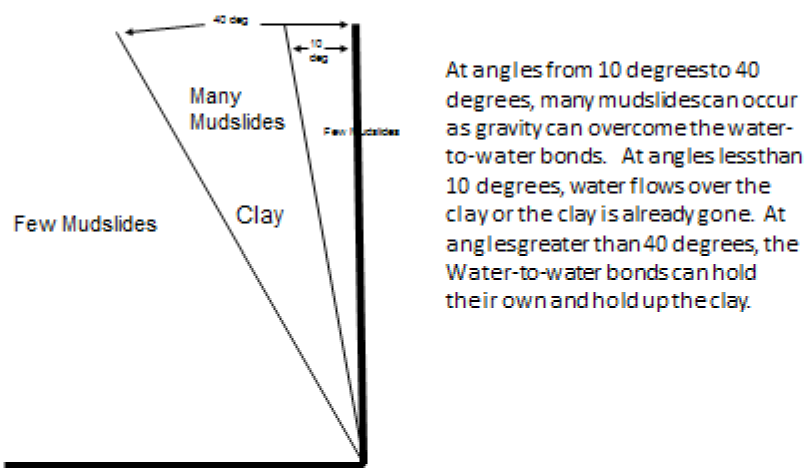

Figure 6.1 (a) Schematic of clay molecule surrounded by water molecules at saturation and chemical bonding of water molecules; and (b) relationship between mudslide occurrence likelihood and vertical angle of the clay surface.

6.3 Satellite techniques

6.3.1 Technological advances

Nowadays, space-borne instruments, such as visible/infrared (IR) imagers in geostationary satellites, Advanced Very High Resolution Radiometer (AVHRR), passive microwave sounders, infrared sounders, and precipitation radars, have high resolutions that can provide remote sensing data for meteorological and hydrological monitoring. Products include cloud characteristics, humidity sounding and wind vectors. An example of a spaceborne passive microwave sensor is WindSAT. WindSAT is a conically-scanning duel-polarimetric (vertical and horizontal) radiometer specially designed for sensing near-surface winds over the ocean (Adams et al. 2008). Its multi-frequency design also allows retrieval of multi environmental parameters, such as precipitation, at the same time.

Many TC rainfall estimation techniques have been developed using either single or combined instruments. Table 6.2 summarizes the techniques reported in Levizzani et al. (2002).

Table 6.2. Tropical cyclone satellite rainfall estimation techniques.

Instrument	Technique	Details
Satellite (visible & thermal infrared)	Cloud Indexing Methods	Assign rain rate to each cloud type
Satellite (visible & thermal infrared)	Bispectral Methods, e.g., RAINSAT (Lovejoy and Austin 1979; Bellon et al. 1980)	Derive and use the relationship between cold and bright clouds and probability of precipitation
Satellite (visible & thermal infrared)	Life History Methods, e.g., Griffith-Woodley technique (Griffith et al. 1978), Negri-Adler Wetzel (NAW) scheme (Negri et al. 1984), NOAA-NESDIS (National Environmental Satellite Data and Information Service) technique, combined NAW with radar data (Porcù et al. 1999)	Analyze clouds' life cycle
Satellite (visible & thermal infrared)	Cloud model-based techniques, e.g., cumulus convection parameterization (Gruber 1973), cloud model (Wylie 1979), Convective	Use cloud physics in the retrieval process

<<Previous Next>>

	stratiform technique (CST) (Adler and Negri 1988; Anagnostou et al. 1999)	
Satellite (passive microwave imagers)	Enhance precipitation signal by minimizing the effects of surface emissivity on MW measurements (Grody 1984), determine the polarization corrected temperature (PCT) and criteria for rain/no-rain boundary (Kidd 1998)	Use the strength of precipitation signal and emissivity of hydrometeors
Satellite (passive microwave sounders)	An algorithm that based on scattering indices (Grody et al. 1999)	Derive atmospheric sounding
Precipitation radar (PR)	An algorithm to get Z-R/Z-A relationship (R = rain rate, A = radar attenuation, Z = reflectivity) (Iguchi et al. 2000)	Get the vertical distribution of rainfall
Satellite (infrared and microwave)	Statistical probability matching between precipitation levels from the Special Sensor Microwave/Imager (SSM/I)+TMI algorithms and brightness temperature (TB) from geostationary satellites (Turk et al. 1998, 2000). Microwave IR Rainfall Algorithm (MIRA) (Todd et al. 2001), Microwave/Infrared Rain Rate Algorithm (MIRRA) (Miller et al. 2000), Precipitation Estimation from Remotely Sensed Information using Artificial Neural Networks (PERSIANN) (Hsu et al. 1997; Sorooshian et al. 2000), Auto-Estimator technique (Vicente et al. 1998)	
Satellite (passive microwave) and PR	Multispectral data from GOES and Tropical Rainfall Measuring Mission (TRMM) PR data (Bellerby et al. 2000)	Estimate rain profile using PR reflectivity (Haddad et al. 1997)
Lightning detection	Combine cloud-to-ground lightning and satellite IR data.	Lightning positively correlates with ice scattering intensity in

<<Previous Next>>

		high frequency microwave radiometry.

Looking to the future, efforts to support the development of satellite remote sensing techniques are pursued under the following two projects:

1) Hurricane Imaging Radiometer (HIRAD) by NASA MSFC/NOAA HRD

It is a C-band passive microwave radiometer, an extension of the Stepped Frequency Microwave Radiometer (SFMR), deployed for tropical cyclone measurements. It will produce imagery of ocean surface wind parameters and rain rates under high winds and heavy rain conditions that often hamper the observational capabilities of higher frequency passive microwave radiometers or scatterometers (Hood et al. 2008, El-Nimri et al. 2008).

2) Geostationary Synthetic Thinned Aperture Radiometer under the "Precipitation and All-weather Temperature and Humidity" mission (GeoSTAR/PATH) by NASA JPL

A microwave sounder in a geostationary orbit under the mission PATH, GeoSTAR will provide measurements including hemispheric 3-D temperatures, humidity and cloud liquid water fields, rain rates and totals, tropospheric wind vectors, sea surface temperatures, and parameters associated with deep convection and atmospheric instability (Lambrigtsen et al. 2008).

6.3.2 Quantitative precipitation estimation (QPE)

Satellites provide means to monitor tropical cyclones and collect information for data assimilation and tropical cyclone rainfall climatology formulation. QPE can be obtained by processing satellite data and conventional surface observation together (Chen et al. 2006). Many QPE techniques using satellite data have been developed around the world. Techniques involve model forecasts, ensemble methods, empirical models, statistical schemes, or combined statistical-dynamical approaches. Some products are available online for references. Examples are Climate Prediction Center (CPC) morphing method (CMORPH) (Joyce et al. 2004), and inversion-based algorithm using TRMM TMI and PR data (Jiang et al. 2006). Table 6.2 also includes techniques used for QPE.

Four techniques*, namely CMORPH, PERSIANN, NOAA/NESDIS Hydro-Estimator and GPM, are highlighted below.

1) NOAA CPC MORPHing method (CMORPH)

CMORPH is a technique based on geostationary satellite cloud motion winds that advect microwave-derived precipitation retrieved at irregular hours forward and backward in time, in order to yield a spatial-temporal consistent precipitation analysis. Meanwhile, precipitation features are "morphed" during the forward and backward propagation (Figure 6.2). CMORPH allows precipitation estimate inputs from any microwave satellite. Products from CPC have resolutions from 8 km to less than 30 km (1/4 degree). However, there is a latency problem for CMORPH. Products are only available about 18 hours from the observation time. A similar product called QMORPH has since been developed. QMORPH has no morphing and can be available within three hours from the observation time (http://www.cpc.noaa.gov/products/janowiak/cmorph_description.html). A study by Joyce et al. (2004) showed that in terms of spatial correlations and equitable threat scores for cases in Australia and the United States, outputs using CMORPH performed better than those using other techniques, such as IR-derived precipitation when there was no passive microwave data available, and MWCOMB (a daily average of all available microwave-derived precipitation estimates without morphing).

2) Precipitation Estimation from Remotely Sensed Information using Artificial Neural Networks (PERSIANN)

PERSIANN has been developed at the University of Arizona using an artifical neural networks (ANN) model with a resolution of 0.25 degree (Hsu et al. 1997). The model estimates rainfall rates based on infrared satellite imagery and using ground-based data to update the ANN parameters. Hsu et al. (1997) demonstrated that the model was able to provide insights into the nature of the physical processes and the diverse precipitation characteristics in response to such processes.

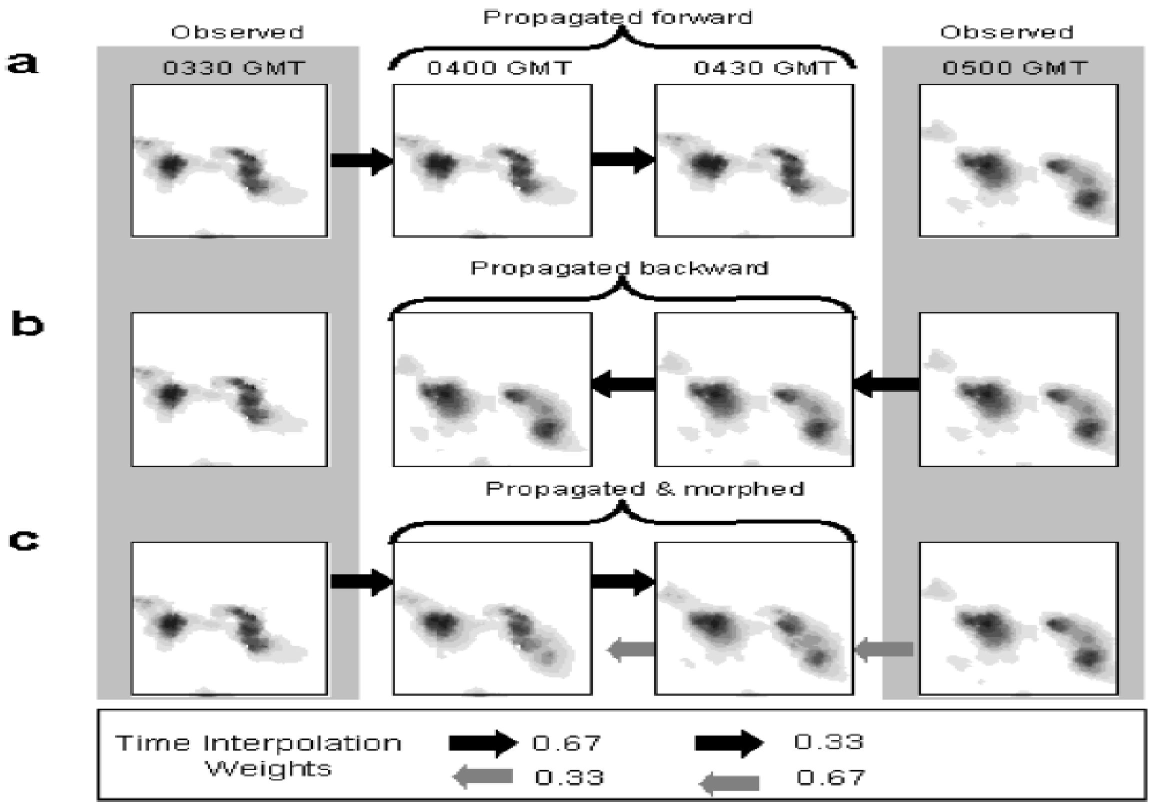

Figure 6.2 Schematic of the morphing process: analyses at 0330 and 0500 UTC are actual passive microwave rainfall estimates; (a) forward propagation from 0330 UTC with linearly decreasing weighting; (b) backward propagation from 0500 UTC with linearly decreasing weighting; (c) derived morphed rainfall fields for 0400 and 0430 UTC (extracted from Joyce et al. (2004)).

---

* *Other notable satellite-based rainfall analyses include (i) TRMM Multi-satellite Precipitation Analysis (TMPA) by NASA; (ii) the blended satellite technique by NRL and (iii) GSMaP by JAXA. Pls. refer to Chan & Chan (2010) for the references.*

3) NOAA/NESDIS Hydro-Estimator

This algorithm outputs rainfall rate and rainfall estimate for the United States only. It is developed based on the auto-estimator algorithm using the brightness temperatures of geostationary satellites and NWP models.

4) Global Precipitation Measurement (GPM) mission

The Global Precipitation Measurement, or GPM, mission will be launched in 2014. It will use an international constellation of satellites to study global rain, snow and ice to better understand climate, weather, and hydrometeorological processes. The GMI instrument, a multi-channel, conical-scanning, microwave radiometer, will measure Earth's atmospheric moisture with near-global coverage. The GMI Flight Unit 2 is planned to fly on a GPM partner-provided spacecraft in a low-inclination orbit as part of the GPM constellation with a targeted launch date of 2014. It will contribute to GPM by enhancing monitoring of TCs and mid-latitude storms and improving estimates of rainfall accumulation.

To validate the satellite rainfall estimates, the International Precipitation Working Group (IPWG) provides a portal on the inventory, reports, information on validation and training on its website (http://www.isac.cnr.it/~ipwg/). It carries out a project that compares and validates daily outputs of different satellite algorithms. Forecasters can make use of the information and choose the appropriate algorithm outputs. Details of the project, information about resources and materials on the techniques and performances of different algorithms can be accessed through the website: http://ipwg.isac.cnr.it/algorithms/inventory/docs/MiRS_Algorithm_Desc_IPWG.doc

6.3.3 Flood monitoring

Other than the meteorological aspects, satellites are also used to monitor flooding, with products available at different spatial and temporal resolutions. Landsat Enhanced Thematic Mapper Plus (ETM+) is able to provide information on the flooded areas which can be differentiated from other types of land cover. However, it has a poor temporal resolution (16 days) and its monitoring capability can be compromised by clouds. Flooding events that last less than two weeks could well be missed (Sandholt et al. 2003). ERS Synthetic Aperture Radar instrument (SAR) can penetrate clouds and produce maps at a local to regional scale. However, similar to Landsat ETM+, its temporal resolution is poor (35 days). As such, neither Landsat ETM+ nor ERS SAR can be used to monitor flood propagation.

NOAA AVHRR images can provide better temporal coverage for flood mapping and analysis of flood propagation at the expenses of the spatial resolution. To address the problem of limited spatial resolution of satellite images, Buckley et al. (2009) used NASA Advanced Microwave Precipitation Radiometer (AMPR) to detect surface water and flooding. The study investigated three flooding events associated with TCs. It was found that that AMPR demonstrated high resolution detection of anomalous surface water and flooding in many situations with sufficiently detailed analyses.

MODIS data can be used in flood analysis and monitoring using different algorithms and techniques (Brakenridge and Anderson 2006). For example, to identify water pixels, a threshold approach and NDVI band ratio [(band2-band1) / (band2+band1)] values can be applied. The water discharge can then be correlated with the radiance threshold to trigger flood alarm (Figure 6.3). In addition, MODIS data can be readily used in GIS to facilitate disaster reduction and mitigation efforts.

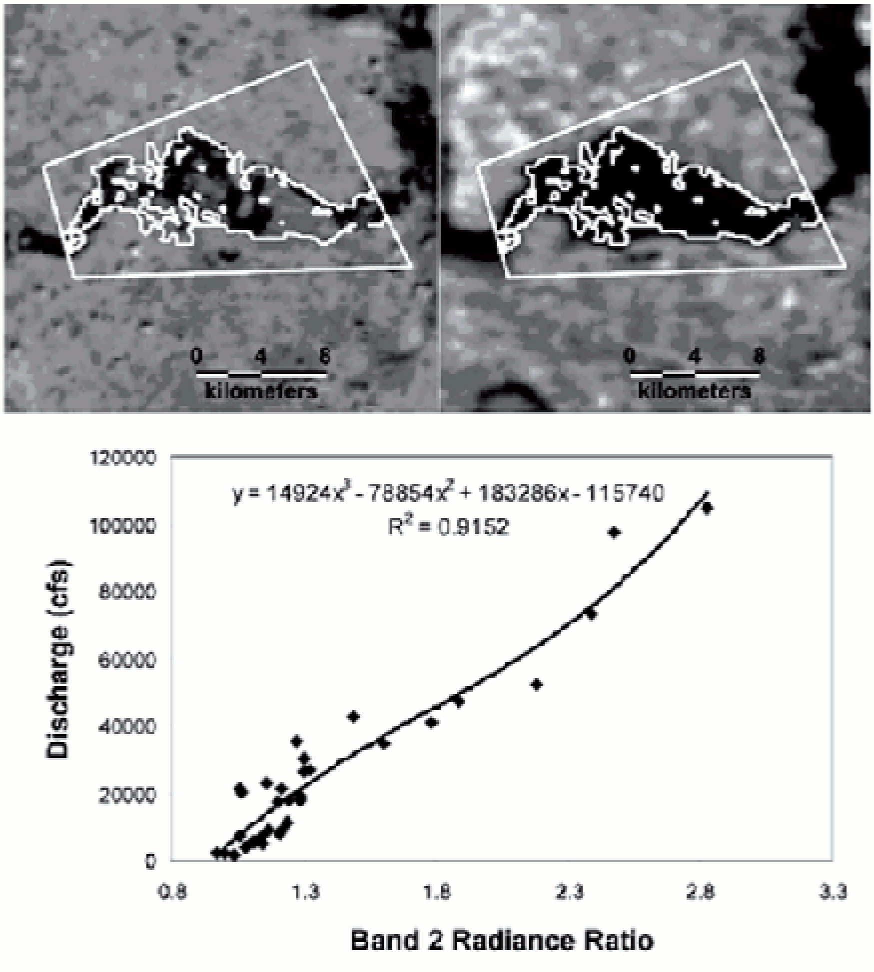

Figure 6.3 Top: MODIS band 2 images during minor flooding (left) and major flooding (right); bottom: MODIS band 2 calibrated radiance ratios versus the water discharge (extracted from Brakenridge and Anderson (2006)).

6.4 Radar techniques

6.4.1 Overview

To improve the understanding of TCs and their rain distribution, radars bearing various functions and techniques have been developed, including the U.S. National Oceanic and Atmospheric Administration (NOAA) WP-3D tail airborne Doppler radar, the Weather Service Radar (WSR) 1988-Doppler (WSR-88D) radar network and portable Doppler radars (Marks 2003). The WSR-88D is now a Dual Polarity (Dual-Pol) radar that has expanded capabilities in better discerning heavy rain, hail, and tornado debris. Along with space-borne radar systems such as NASA TRMM, land-based and satellite-based radar data can be used together for enhanced analyses of temporal as well as spatial rain variability.

<<Previous Next>>

Keeping pace with the evolution of radars, different algorithms have been developed to provide better rain estimates using radar signals, to study the rain characteristics, and to facilitate the design of nowcasting tools.

6.4.2 Radar quantitative precipitation estimates (QPE)

Radar QPE algorithms can be categorized into two types, the linear/non-linear regression methods and the probability matching methods. Medlin et al. (2007) studied the rainfall associated with a stationary weak hurricane Danny using WSR-88D system and the WSR-88D precipitation rate algorithm. It was found that the radar estimate with capping maximum precipitation rate and a static Z-R relationship would lead to an under-estimation of rainfall. Li and Lai (2004) adopted a dynamic update of Z-R relations using real-time raingauge measurements. This dynamic approach allowed the Z-R calibration process to evolve as the rain event unfolded, hence leading to more realistic rainfall assessment for nowcasting applications. Figure 6.4 illustrates the dynamic radar-raingauge rainfall re-analysis process.

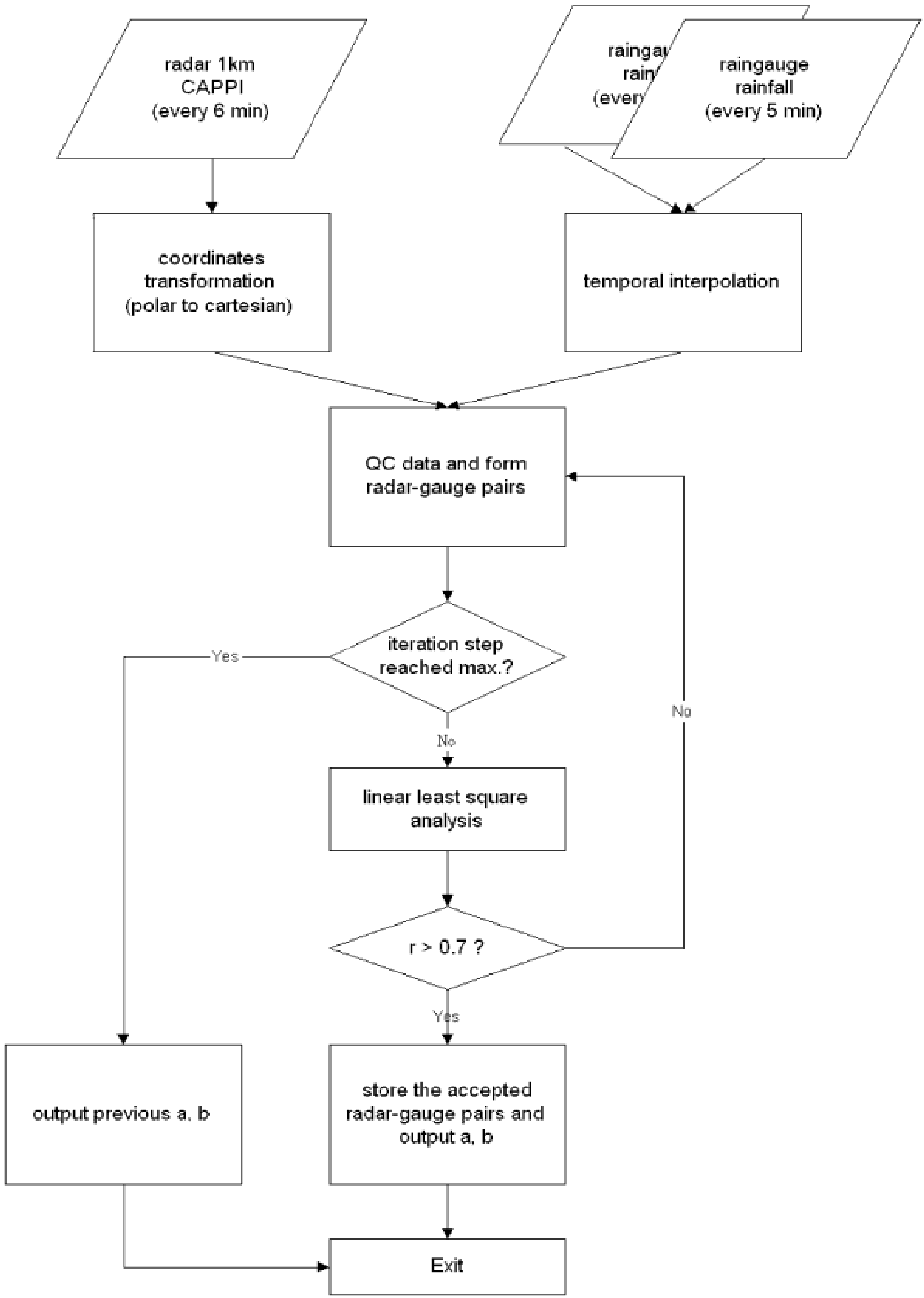

Figure 6.4 Flowchart of dynamic Z-R update process (extracted from Li and Lai 2004).

<<Previous
Next>>

6.4.3 Rain characteristics

On the NOAA WP-3D, there are Stepped Frequency Microwave Radiomater (SFMR), tail radar, lower fuselage radar and the Knollenberg Particle Measurement System Optical Array Spectrometer Probe (Jiang et al. 2002). Data from different instruments allow the study and validation of precipitation and rainband characteristics inside TCs, and facilitates the analysis of the evolution of cyclones' kinematic structure. Such studies greatly facilitate the understanding of the weather associated with landfalling TCs. Findings can also be used for the HIRAD data mentioned in Section 6.3.1.

6.4.4 Future development

The development of NEXRAD in Space (NIS), a sophisticated Doppler precipitation radar at Ka-band frequency mounted on a GEO satellite platform, can provide observations and better understanding of rain microphysics and kinematics within tropical cyclones (Smith et al. 2008).

To provide better radar-based QPF, data assimilation techniques incorporating radar QPE, cloud analyses from radars and satellite observations are being developed for mesoscale non-hydrostatic models (e.g., assimilation of radar QPE in JMA JNoVA-4DVAR) and mesoscale ensemble prediction system.

Regional mobile X-band dual-polarimetric radars have the capacity to provide more reliable QPE. Data so derived can also be used to validate models and improve QPE.

6.5 Raingauge networks and techniques

6.5.1 Gauge-based statistical models

TC rainfall rates and distributions can be derived from raingauge/satellite climatology and persistence, and used as input for forecast models.

Rainfall Climatology and Persistence (R-CLIPER) is a gauge-based statistical model with radial distributions of rainfall, assuming symmetric rainfall pattern. Raingauge data are first grouped into annuli around the cyclone centre. The mean rainfall rate of each annulus is calculated and taken as the climatology. Rainfall associated with the cyclone was deduced according to its intensity. R-CLIPER rainfall can then be used to validate numerical outputs and improve the models.

Marks et al. (2002) refined the gauge-based R-CLIPER model by using the microwave imager (TMI) rainfall estimates from the NASA TRMM satellite, i.e. a satellite-based R-CLIPER model, on the basis that the satellite-based climatology and the gauge-based climatology had similar mean rainfall rates in the radial direction. TMI data provide a global coverage and overcome the problem of sparse gauge data near the cyclone centre. Lonfat et al. (2004) further investigated the cyclone rainfall rates and distributions using the 3-year TMI data. A conditional (only when raining) probability density function (PDF) of rain rate occurrence (area) was constructed for each annulus within 500 km of the cyclone centre (Figure 6.5). Combining PDFs of different annuli, a contoured frequency by radial distance (CFRD) diagram was produced (Figure 6.6). Lonfat et al. (2004) re-calculated the PDFs by "weighing each rain estimate by the corresponding rain rate" and then "normalized to the total amount of rain" to get the rainfall flux. A CFRD for rainfall flux is shown in Figure 6.7. In the CFRD, a broader PDF indicates higher degree of asymmetry.

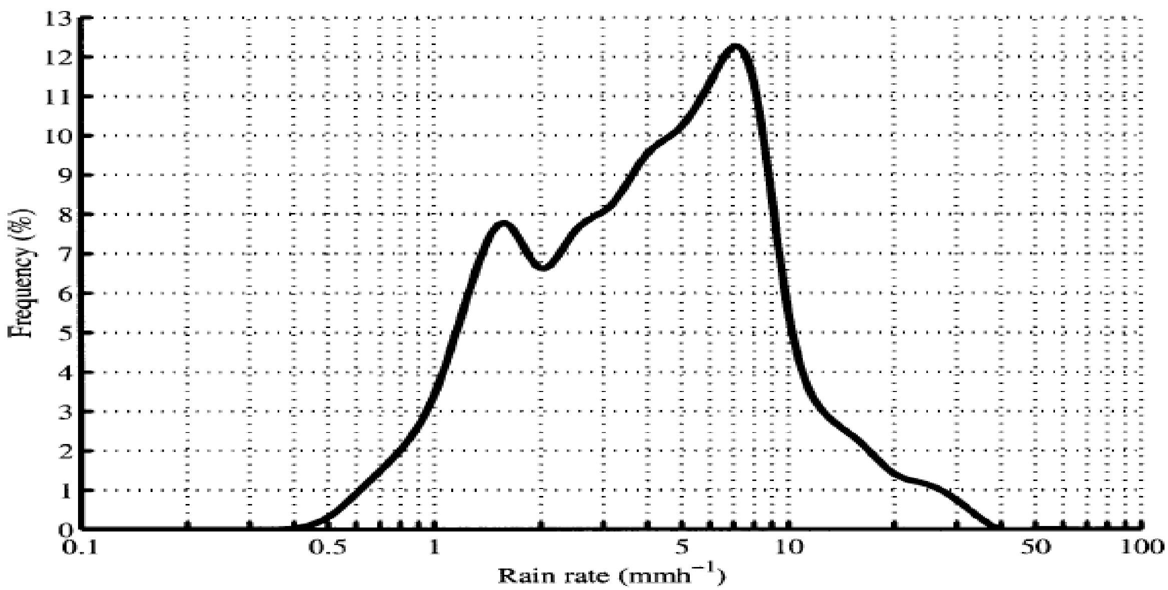

Figure 6.5. PDF of rainfall for Hurricane Dennis within 300 km from the storm center (extracted from Lonfat et al. 2004).

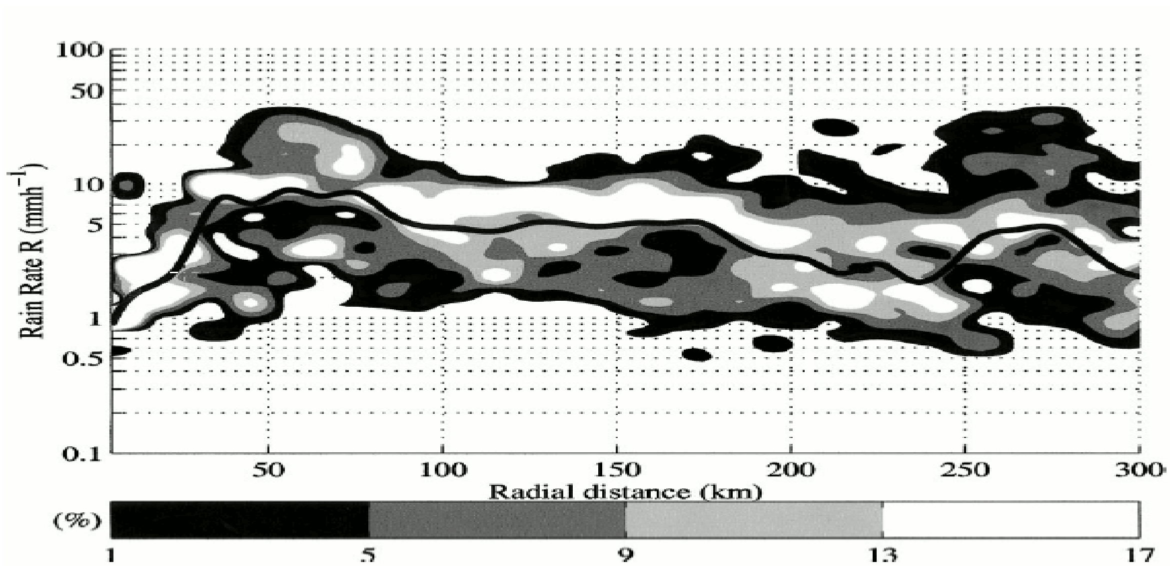

Figure 6.6. Rain rate CFRD for Hurricane Dennis. (extracted from Lonfat et al. 2004)

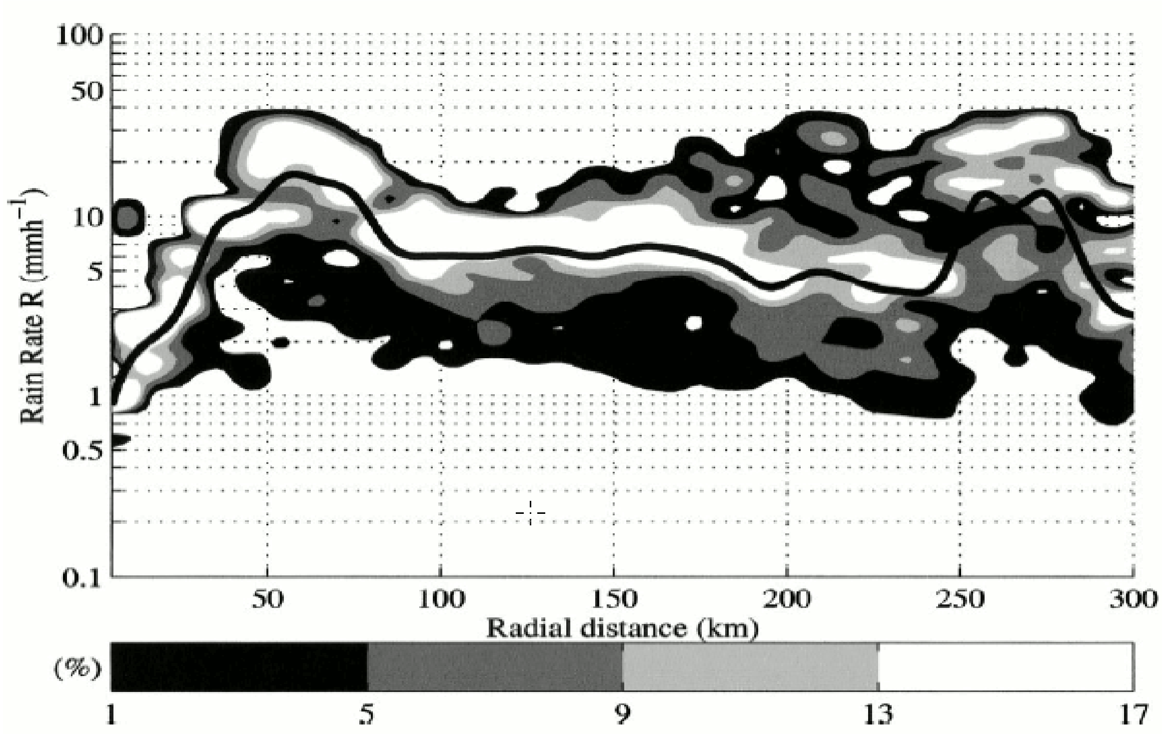

Figure 6.7. CFRD for rainfall flux for Hurricane Dennis (extracted from Lonfat et al. 2004)

CFRDs can be constructed according to cyclone intensities. Lonfat et al. (2004) found that for cyclones with higher intensity, the mean rain rate increased, location with peak rainfall rate became closer to the cyclone centre, and the spread of the PDF narrowed. This refined R-CLIPER model can predict rainfall rate of a particular time step, which can be integrated along the cyclone track and used to produce the accumulated rainfall.

6.5.2 Asymmetry and topographic effects

To forecast the change of rainfall rates after landfall, an inland decay model was proposed by Marks et al. (2002):

$$R(r,t) = (ae^{-\alpha t} + b)\, e^{-(r-r_m)/r_e}$$

where r is radius and t is time; a and α are defined by fitting raingauge data in time; b is defined by fitting rain gauge data by radius; r_m = radius of maximum rainfall; r_e = 500 (km)

Tuleya *et al*. (2007) proved that the gauge data and TMI data radial profiles for tropical storms and category 1 and 2 hurricanes had remarkable agreements. Correlation coefficients between them were more than 0.95. The R-CLIPER model with TMI climatology can be represented by equations below:

<<Previous Next>>

$R(r) = R_0 + (R_m - R_0)(r/r_m) \quad r < r_m$

$R(r) = R_m \exp(-(r - r_m)/r_e) \quad r \geq r_m$

where R_0 and R_m are the mean rainfall rates at $r = 0$ and r_m (radial extent of the inner-core rain rate) respectively; r_e (radial extent of the tropical system rainfall).

As it is based on climatological values, the R-CLIPER model generally fails to give extreme values. Tuleya et al. (2007) adjusted the TMI rain rate in the R-CLIPER model as a function of radius and maximum wind speed and incorporated the modified R-CLIPER model into the operational version of the Geophysical Fluid Dynamics Laboratory (GFDL) hurricane model.

The modified R-CLIPER model was capable of forecasting higher rainfall amount as it took the maximum wind speed into account. Forecast rainfall from the modified R-CLIPER model proposed by Tuleya et al. (2007) were verified against 32,784 daily gauge observations from 25 TC cases. The modified R-CLIPER model performed slightly better with a smaller mean absolute error than using the GFDL model. However, the modified R-CLIPER model still under-estimated the total rainfall amount while GFDL model tend to over-estimate and had high biases at all thresholds.

TC rainfall distribution depends on various factors, such as cyclone intensity, location, translation speed, wind shear (Lonfat et al. 2004) and topography (Lonfat et al. 2007). The R-CLIPER model assumes azimuthally symmetric rainfall distribution, which is one of its limitations. Lonfat et al. (2004) investigated the asymmetric component by using the first-order Fourier decomposition of the annulus rainfall estimates. It was found that higher rainfall rate was generally located ahead of the TC center. Quadrants with higher rainfall rates shifted from the front-left to front-right with increasing cyclone intensity. **Geographically, TCs in the Northern Hemisphere had rainfall rate peaking in the front-right quadrant, while those in the Southern Hemisphere peaked in the front-left quadrant.**

Lonfat et al. (2007) improved the R-CLIPER model further by parameterizing shear and topography to form the Parametric Hurricane Rainfall Model (PHRaM).

$R_{PHRaM} = R_{R\text{-}CLIPER} + R_{shear\ mod} + R_{topography}$

Impact of vertical shear is represented by wavenumber-1 and -2 Fourier coefficients:

$R_{shear\ mod}(r,\alpha) = \Sigma c_i(r)\cos(i\alpha) + \Sigma d_i(r)\sin(i\alpha)$

where r is the radial distance and α is the azimuthal angle.
Rainfall amount forecast in the R-CLIPER model is re-distributed spatially in the PHRaM model to reflect the asymmetry.

Topography effect is parameterized by using: $R_{topography} = c\vec{V}_s \bullet \nabla h_s$

where c is a constant, V_s is the surface (10m) wind field; and h_s is the ground elevation.
It is found that PHRaM model outputs have higher equitable threat score than the R-CLIPER model outputs. Both the mean cyclone total rainfall and the rain flux PDF from the PHRaM model are closer to the observation.

Instead of PHRaM, Cheung et al. (2008) used another statistical method based on rainfall climatology in Taiwan as the rainfall pattern and amount in Taiwan were found to be highly related to the topography. Climatology rain rate distribution maps corresponding to the cyclone locations in the vicinity of Taiwan were constructed (Figure 6.8).

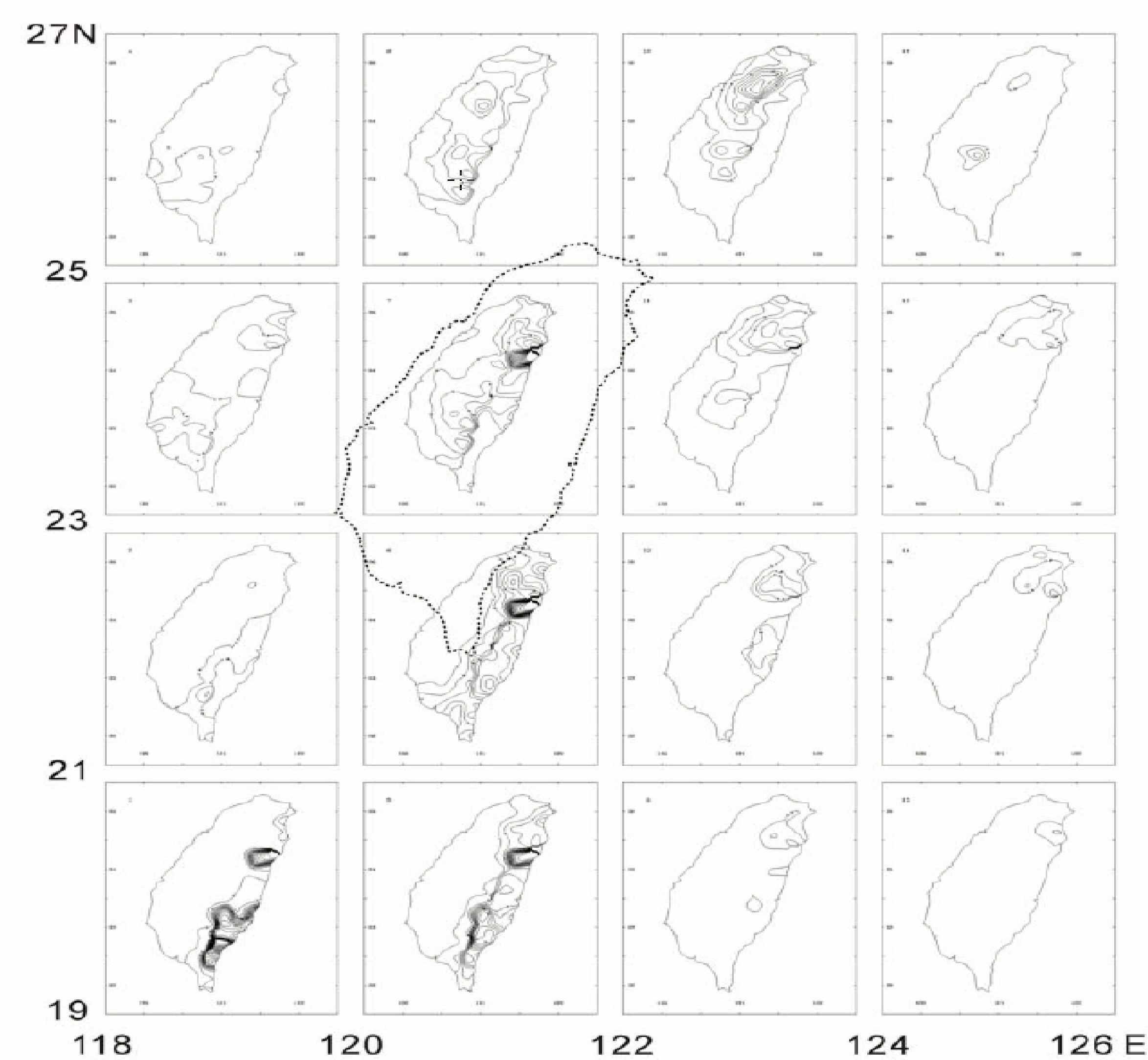

Figure 6.8. TC rainfall climatology in the Taiwan area (contours shown are hourly rain rate with interval 2 mmh-1). Each 2°x2° latitude/longitude panel represents the rain distribution when the TCs are located in that panel relative to the central Taiwan map (extracted from Cheung et al. 2008).

<<Previous Next>>

Temporal characteristics of rainfall were studied by Cheung et al. (2008) using cluster analysis. Results of the study showed that the clusters were geographically related. As a result, there was a reasonably good performance in terms of correlation coefficients (> 0.6) for the estimation of accumulated rainfall amount up to a duration of six hours. Equitable threat scores for 24-hour rainfall were higher (0.4 - 0.5) in northwestern Taiwan than those in the southern part. However, there was serious under-estimation of 24-hour rainfall amounts that exceeded 130 mm.

6.6 Synoptic and climatological techniques

6.6.1 Climatological patterns

Cerveny and Newman (2000) suggested that by constructing climatological relationships between TC parameters and rainfall, "seasonal predictive climatic parameters" could be identified. Based on historical rainfall data categorized into a 2.5°x 2.5° grid, two databases were generated for study: (a) total tropical cyclone rainfall aggregated over the nine grids surrounding the averaged daily cyclone positions; and (b) inner core rainfall from the central grid over the averaged daily cyclone positions. Linear relationships were found between cyclone intensity and rainfall amount for TCs over the North Pacific and the Atlantic basins. More intense cyclones generally produced more rain. The daily rainfall accumulation, as well as the ratio of inner core rainfall to the total rainfall, were both related to the cyclone's daily maximum surface wind speeds. Such relationships could potentially be used as forecast aids for operating heavy rain and flood warnings.

Rodgers et al. (2000 and 2001) used the derived mean monthly rainfall amounts of the SSM/I instruments onboard of the DMSP satellite to study the spatial and temporal features of TC rainfall over the western North Pacific and the North Atlantic. From these studies, it was found that TC rainfall (within four degrees of cyclone centres) generally increased during the El Niño years over the North Pacific but decreased over the North Atlantic. In the North Pacific, increase of rainfall in the eastern part was attributed to the higher SSTs, but the rainfall increases in the western and central parts were apparently not as closely related to the relative changes in SSTs and were probably more the result of corresponding changes in the general circulation patterns such as the migration of ITCZ. Jiang and Zipser (2010) used the TRMM data instead for studying TC rainfall (within 500 km of cyclone centres) over six basins around the globe. Similarly, **rainfall increases were observed over the North Pacific during the El Niño years.** Changes in TC rainfall were nearly neutral over the south Indian Ocean and the South Pacific, but decreased over the North Atlantic and the north Indian Ocean.

Spatially, rainfall associated with the cyclone's inner core was generally representative of the cyclone's total rainfall (Cerveny and Newman 2000). Moisture availability in the subtropics might explain the latitudinal variation of rainfall based on the combined data for the North

Atlantic and North Pacific basins. TC rainfall zonal maxima were located poleward (5°-10°) of non-TC rainfall maxima over both basins (Rodgers et al. 2000 and 2001).

Temporally, TC rainfall in the North Pacific reached a maximum in late summer and early autumn (Rodgers et al. 2000). The lag behind the months of maximum insolation was more pronounced in the western part than in the central and eastern parts. The lag was attributed to the maximum warming of the SSTs and the favourable general circulation patterns in early autumn for cyclogenesis and cyclone intensification. However, Cerveny and Newman (2000) found that TCs in the North Pacific in November and December would bring more rain as they generally occurred in the low latitudes with higher SSTs. They also showed that rainfall usually peaked around six days after cyclone formation.

6.6.2 Rainfall patterns in and around the cyclone

TC rain can generally be separated into two types: stratiform and convective rain. Yokoyama and Takayabu (2008) investigated the stratiform rain ratio (SRR) and rain type spatial structures in TCs using the TRMM data. In the study, SRR was defined as "the ratio of the stratiform rainfall to the total rainfall" and rain-top height (RTH) was defined as "the highest altitude with a threshold of 0.3 mm/h in the rain-detected pixels". The mean SRR for TCs (52%) was found to be larger than the equatorial oceanic mean (44%). RTH of TCs was concentrated in the range of 7-9 km; RTH of stratiform and convective rain at ~7.5 km and ~8.5 km respectively contributed most to TC rainfall.

The spatial distribution of stratiform and convective rain was also analyzed. The "inner core", i.e., 0-60 km from the cyclone centre, had small SRR and high RTH. Rain was mainly associated with convective activity with RTH around 8-12 km in the mature cyclone stage. Rain in the "rainband", i.e., 60-500 km from the cyclone centre, had large SRR and relatively large rain yield, suggesting large rainfall amount with moderate convective activity. Rain mainly came from regions with RTH around 6-9 km in the mature cyclone stage. An "inner rainband", situated between 80 and 230 km (90 and 140 km) from cyclone centres, also had large SRR for tropical cyclones with the maximum sustained winds greater than 64 kt/119 km/h (128 kt/237 km/h). Between the "inner core" and the "inner rainband" was a mixed zone of eyewalls and rainbands, depending on the eyewall radius, and at times, eyewall-replacement cycles.

While significant rainfall occurs invariably close to or in the vicinity of TCs, less attention is paid to enhanced rainfall while a TC is still far away or when it is dissipating. Interactions between TCs, which act as moisture suppliers, and other synoptic systems would also bring significant indirect precipitation to remote areas. Wang et al. (2009) used the Advanced Research version of the Weather Research and Forecast (WRF) model to simulate Typhoon Songda (2004) at high resolution to investigate the cyclone's influence on the environment circulation, as well as its effect on precipitation in far-away places such as Japan. While Songda was still southeast of Okinawa, heavy precipitation already occurred over parts of Japan and the adjacent seas. The numerical experiments demonstrated that Songda's outer circulation helped to enhance the southerly winds. Moisture was advected polewards and resulted in moisture flux convergence further downstream. Wang et al. (2009) found that at one stage Songda contributed more than 90% of the rainfall over the area under study.

As a TC dissipates, its remnant will interact and become increasingly affected by large-scale weather systems. Spatial differences in rainfall patterns and amounts can be quite large. For TCs from 1992 to 2004 studied by Ritchie and Szenasi (2006), those that fully interacted with mid-latitude systems had rainfall patterns that appeared similar to those produced by mid-latitude troughs. ain would be brief but heavy. In the absence of mid-latitude troughs in the vicinity, rainfall patterns varied. A slow-moving cyclone remnant could bring persistent and widespread rain.

Environmental forcing, such as vertical wind shear, can affect the rain rate and rainfall asymmetry. Quinlan (2008) decomposed the shear vector into u- and v-components and analyzed the rain rate for Hurricane Emily (2005). There was "significant positive correlation" between the u-component of the shear vector and rain rate over the northwestern and northeastern quadrants in the vicinity of the cyclone. Lonfat et al. (2004) further analyzed the azimuthal rainfall distribution of Hurricane Dennis (1999) using TRMM observation. **It was found that rainfall rates increased on the left and front-left of the cyclone centre in the inner 150 km (81 nmi). Outside the 150 km (81 nmi) region, the outer rainbands concentrated on the front and front-right of the cyclone centre**. Gao et al. (2009) examined the vertical wind shear effect on asymmetric rainfall distributions using the mean wind difference between 850 hPa and 200 hPa over a 200-800 km (108-432 nmi) annulus from the centre of Typhoon Bilis (2006). **Rainfall was found to increase downshear right in the outer rainbands.** The study explained the phenomenon using vortex tilting and vorticity balance.

6.6.3 Orographic effect and landfall

Hurricane Dean brought heavy rain to the mountainous island of Dominica in the West Indies in 2007. Smith et al. (2009) used rain gauges, MODIS images, and radar scans to study the terrain's effect on precipitation. Assuming typical trade-wind inversion and through a Froude number assessment, it was considered that high wind speeds within the hurricane environment would not be conducive to convection triggering by terrain. As such, enhanced convection that brought twice as much rainfall to the mountainous region was apparently induced by orography through a local seeder-feeder mechanism.

Wu et al. (2009) studied a heavy rain event in the Taiwan area associated with the interaction between Typhoon Babs (1998), the East Asia winter monsoon and terrain using a series of numerical sensitivity experiments. While the interaction between Babs and the winter monsoon gave rise to enhanced low-level convergence, it was found that the terrain of Taiwan played a key role in shaping the low-level convergence patterns. Removal of the terrain also led to different rainfall distribution in the absence of orographic lifting.

To study the potential role played by cyclone motion in modulating the topographic rain, rainfall distributions corresponding to different cyclone track scenarios were thoroughly analyzed by Harville (2009). Cyclone tracks approaching the east coast of the United States towards the southern central Appalachian mountain range were stratified into four types. Rainfall patterns corresponding to different track scenarios provided useful guidance in assessing flooding risks. Similar techniques can potentially be adopted for use in other regions.

Chan et al. (2003) investigated the convection asymmetry of four TCs making landfall along the south China coast in 1999 using radar, satellite and NCEP wind shear data. It was suggested that asymmetric convection first developed in the mid to lower troposphere west of the cyclone. It was then advected to the southward side by the cyclonic flow and rising motion in the upper troposphere.

Rainfall associated with a TC can become asymmetric after landfall. The asymmetry can be due to frictional effect in the boundary layer (maximum convergence in the forward flank right of a translating vortex), vertical wind shear (asymmetric patterns of rainfall closely related to cyclone intensity, magnitude of vertical shear and distance of rain area to the cyclone centre), and topography.

Atallah *et al.* (2007) examined hurricanes making landfall over the United States by separating them into two types: (a) those with precipitation predominantly to the left of their tracks and (b) those with precipitation mostly to the right of their tracks. Evolution of precipitation in these hurricanes were studied using the potential vorticity and quasigeostrophic frameworks. For (a), most of the hurricanes were undergoing extratropical transition. For (b), the hurricanes were interacting with downstream ridges. The contrast was attributed to potential vorticity re-distribution through diabatic heating.

Gao *et al.* (2009) analyzed the mechanism for heavy rainfall associated with Severe Tropical Storm Bilis (2006) after its landfall in China. The study divided the rain events into three stages based on timing and location. Rain during the first stage was directly induced by the inner-core circulation. Moisture, instability and lifting were all important elements for the deep moist convection that took place during the second stage when heavy rain occurred. The third stage was the interaction between Bilis and the South China Sea monsoon, enhanced by topography. Vigorous vertical motion was triggered and sustained by strong vertical shear, warm-air advection, frontogenesis and topography. Since diagnoses of the omega equation, vertical shear, vortex tilting and frontogenesis could be easily applied to any gridded observational analysis or forecast field in real time, they could also be used as forecast guidance on heavy rainfall as the TC moved inland.

6.7 QPF products

6.7.1 Numerical and satellite-based products

Unless a TC comes close to land and is within land-based radar coverage, rainfall assessment has to rely mostly on numerical and satellite-based QPF products. QPF outputs can be in the form of deterministic accumulated rainfall, probabilistic rainfall forecast, rainfall rate and precipitable water.

Increasingly, more and more QPF products are being made available online. They have different spatial coverage, spatial resolution and updated frequency. The NOAA Environmental, Satellite and Data Information Service (NESDIS) has a comprehensive website (http://www.ospo.noaa.gov/Products/atmosphere/rain.html), and two of the products are highlighted below:

1) *Tropical Storm Risk*

Tropical Storm Risk (TSR) of University College London has a graphical quantitative and probabilistic rainfall forecasting application (accessible through the website http://www.tropicalstormrisk.com). It provides forecasts up to five days ahead and updates twice a day for active TCs worldwide. Data for the precipitation forecast comes from the UK Met. Office global model. There are altogether 20 output files for each run: forecast accumulated rainfall for the next 24, 48, 72, 96, and 120 hours and probability forecasts for three rainfall thresholds.

2) *Ensemble Tropical Rainfall Potential (eTRaP)*

This is an ensemble product using POES satellite observations and different cyclone track forecasts. The spatial resolution is 4 km, updated every six hours. Products include deterministic and probabilistic accumulated rainfall forecasts. There are altogether 25 output files for each run: 0 - 6 hr, 6 - 12 hr, 12- 18 hr, 18 - 24 hr, 24 hr total rainfall and probability forecasts for four rainfall thresholds.

eTRaP, a technique derived from Tropical Rainfall Potential (TRaP - Kidder et al. 2005; Ferraro et al. 2005), basically consists of rain rate estimates using data of different microwave sensors. Rain rate estimates from satellites are propagated forward along the forecast TC track assuming both the rain rate and forecast track are accurate. To reduce errors arising from various assumptions, ensemble TRaP (eTRaP) has been brought into operation. Figure 6.9 shows the steps introduced by Ebert et al. (2009). eTRaP consists of TRaPs initialized at various observation times and along different track forecasts. Weights corresponding to sensors and latency are assigned to ensemble members. Both deterministic and probabilistic forecasts are produced. Ebert et al. (2009) compared the performances of eTRaP and TRaP for 6-hours and 24-hour accumulated rainfall. Predicted maximum rainfall, RMSE and correlation coefficient corresponding to eTRaP products were all better than those from TRaP.

Attempts were also made elsewhere to deploy satellite-based QPE for generation of TC QPF, using a method similar to TRaP or eTRaP. For example, QMORPH precipitation estimates, which are similar to CMORPH estimates (Section 6.1.2) except that there is no morphing and the microwave precipitation features are propagated forward in time only (http://www.cpc.noaa.gov/products/janowiak/cmorph_description.html), can be used together with a subjective forecast cyclone track to produce rainfall forecasts. Chan & Chan (2010) advected the 0.25-degree hourly QMORPH rain estimates along the Hong Kong Observatory's subjective forecast cyclone track to obtain a point forecast of the hourly rainfall at the Observatory, as well as daily rainfall over the coast of Guangdong and the northern part of the South China Sea for the next three days. Forecasts are updated every hour and become available about three hours after observation time. The QPF results and products so derived are found to be particularly useful if the cyclone motion deviates from the NWP model forecast.

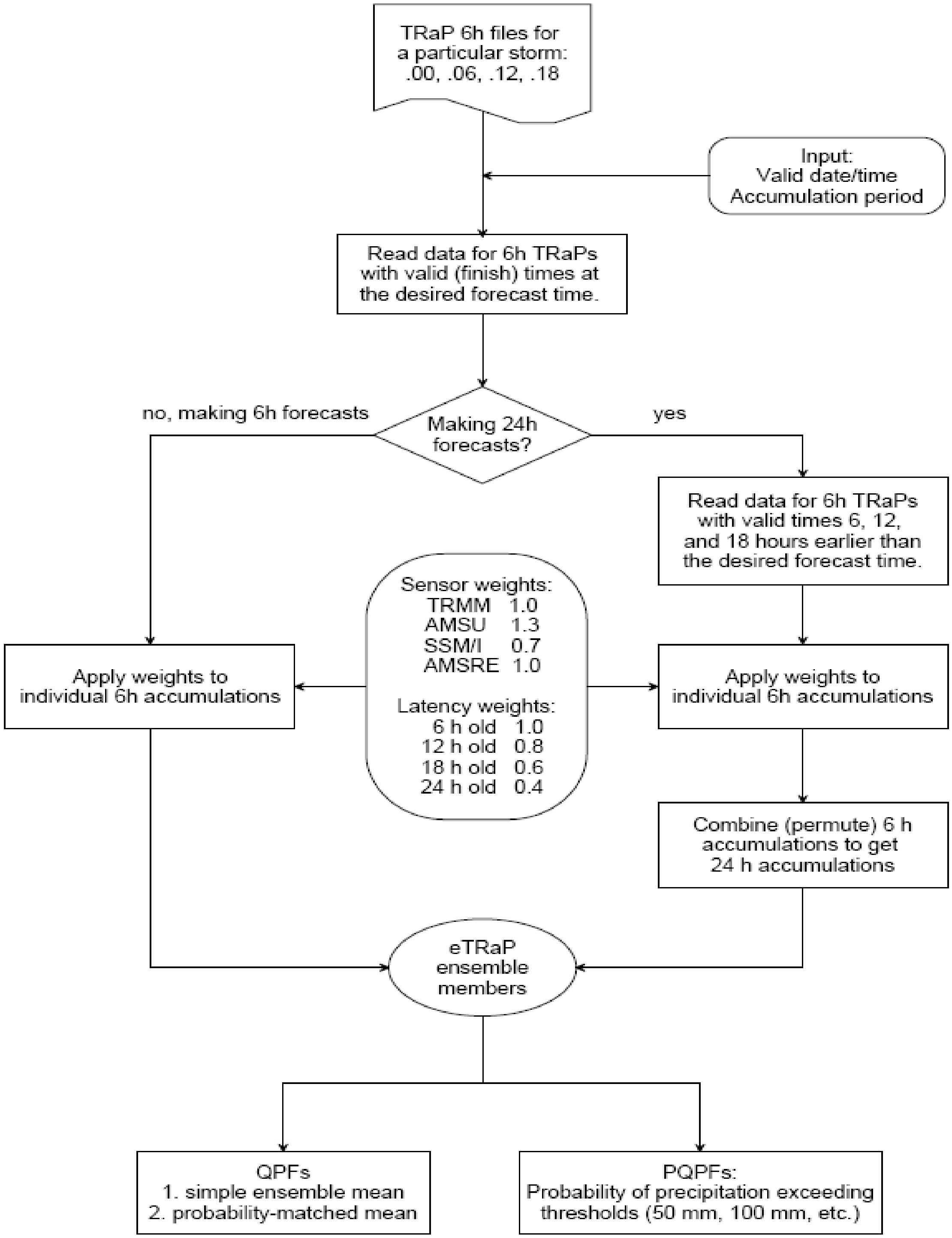

Figure 6.9. Steps in the generation of 24-hour eTraP forecasts (extracted from Ebert et al. (2009))

6.7.2 Multi-model ensemble

Even though NWP models are increasingly becoming the main prognostic tool in operational TC forecasting, model-based QPF guidance is, as yet, not reliable enough for deterministic applications. Useful information is mostly in terms of qualitative trends and probabilistic assessment utilizing a variety of ensemble techniques.

Krishnamurti et al. (2009a and 2009b) used a consensus multi-model forecast product called the FSU super-ensemble for rainfall prediction. The FSU super-ensemble rainfall forecasts were superior to individual members' forecasts and their ensemble mean (Mishra and Krishnamurti 2007, Krishnamurti et al. 2009a and 2009b).

The FSU super-ensemble strategy consisted of two phases: training and forecast phases. The training phase used outputs from ten different models to calculate the statistical weights for each prognostic variable at each grid (both horizontal and vertical), at different time steps and for different member models. "These weights (arose) from a statistical least squares minimization using multiple regressions" (Krishnamurti et al. 2009a), so that a minimum error term *G* was obtained:

$$G = \sum_{i=1}^{N_{train}} \left(S_i^{'} - O_i^{'} \right)^2$$

where N_{train} was the number of time samples in the training phase, and S_t' and O_t' were the super-ensemble and observed field anomalies respectively at training time *t*.

However, only the temporal anomalies of prognostic variables, not the full field, were used. The super-ensemble forecast was constructed as:

$$S = \overline{O} + \sum_{i=1}^{N} a_i \left(F_i - \overline{F}_i \right)$$

where $\overline{O}$ was the observed climatology; a_i was the weight for the *i*th member in the ensemble; and F_i and $\overline{F}_i$ were the forecast and forecast climatological values for the training period respectively for the *i*th model's forecast.

The statistical weights were then used in the forecast phases. Outputs from the same member model were fed into the super-ensemble to obtain the super-ensemble forecasts.

Mishra and Krishnamurti (2007) showed that the FSU super-ensemble forecast provided a robust forecast product up to Day 5 of the rainfall forecasts over the tropics during June-September 2007 in terms of root-mean-square errors, anomaly correlations and equitable threat scores. The equitable threat scores and bias scores both improved further over the Indian monsoon region with the use of downscaling (Krishnamurti et al. 2009a). The FSU super-ensemble products were also found to be very useful for precipitation forecasts for post-landfall heavy rain and flood events in China up to Day 10 (Krishnamurti *et al*. 2009b).

<<Previous Next>>

6.7.3 Radar-based now casting application

Nowcasting techniques using radar QPE can provide radar-based Quantitative Precipitation Forecast (QPF). Li and Lai (2004) and Li et al. (2000) used the Tracking Radar Echoes by Correlations (TREC) technique to track rain echoes (Figure 6.10) and provide QPF in the next three hours using a simple linear advection scheme. The results were found to be generally reliable for TC rainbands that were predominantly driven by the advective process.

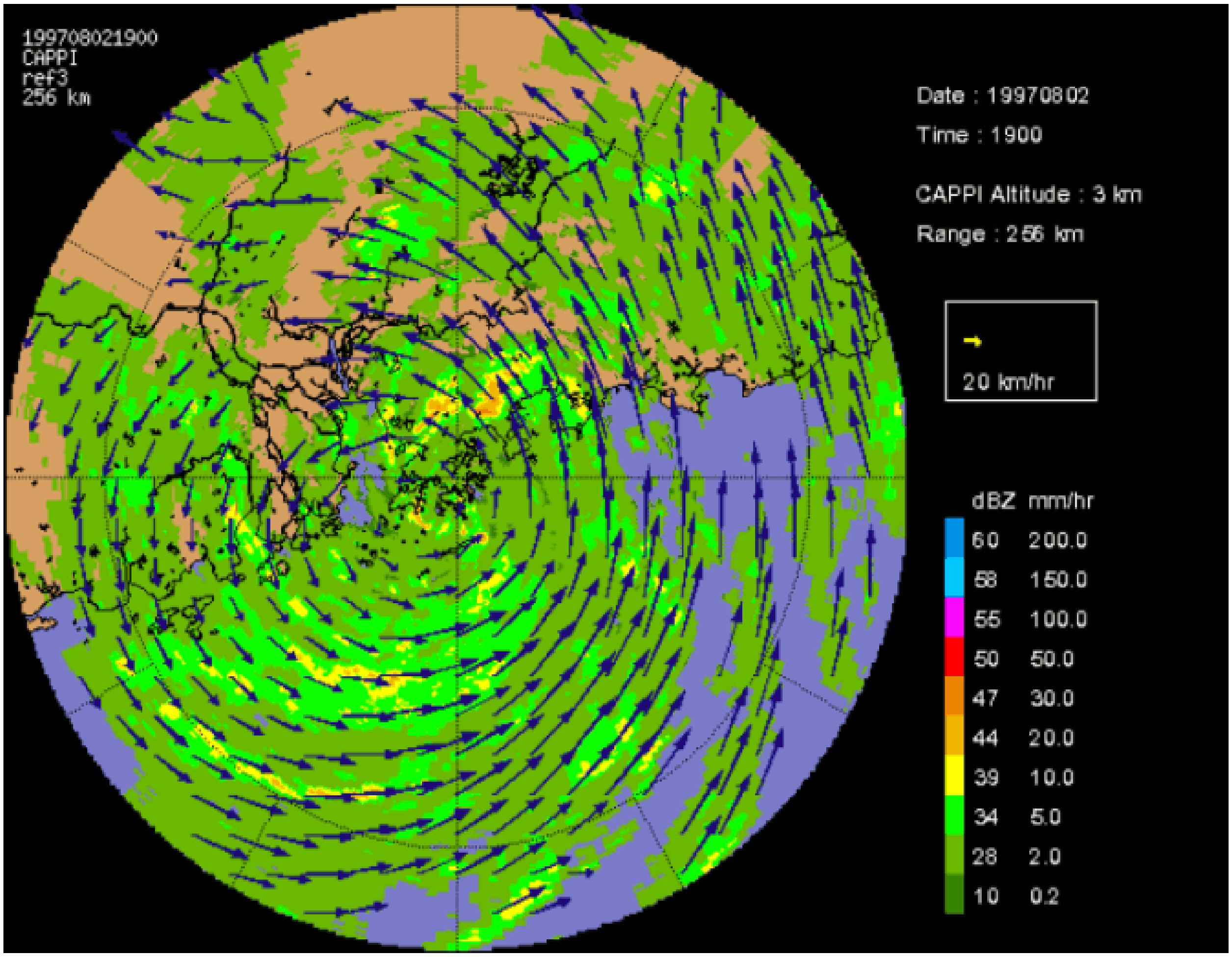

Figure 6.10. TREC vector fields of Typhoon Victor over Hong Kong at 1900 HKT on 2 August 1997 (extracted from Li *et al*. 2000).

Nowcast and NWP blending technique can also be used. Lai and Wong (2006) adopted a modified semi-Lagrangian advection scheme to replace the TREC technique for echoes advection. QPF outputs using the modified advection scheme were then blended with numerical model outputs.

6.7.4 Verification

Given the QPF limitations, well-validated performance assessment and verification statistics allow forecasters to apply the QPF products judiciously and intelligently. Marchok *et al*. (2007) developed a scheme for validating QPFs for landfalling TCs. Cyclone-total rainfall forecasts by the NCEP operational models, i.e. the Global Forecast System (GFS), the Geophysical Fluid Dynamics Laboratory (GFDL) hurricane model, the North American Mesoscale (NAM) model, and the Rainfall Climatology and Persistence (R-CLIPER) model were studied and compared for all landfalling TCs affecting the United States from 1998 to 2004. In the study, three attributes were used for verification: (1) ability to match the observed rainfall patterns; (2) ability to match mean values and amounts of observed rainfall; and (3) ability to produce extreme amounts of rain. They found that GFS performed the best among all studied models for all attributes. Other models tend to over-predict heavy rain or under-forecast rain at a distance away from the cyclone track. Marchok *et al*. (2007) implemented a technique in the verification exercise to remove the impact of track errors on QPF skill. It was found that R-CLIPER, GFDL and NAM models all had QPF skill improvements. Skills of the GFDL and NAM models became comparable to GFS. Armed with such information, forecasters could assign weights on various QPF products according to their operational assessment.

Brennan *et al*. (2008) demonstrated improvement in QPF skill when forecasters' experience was included. Verifications were conducted for 24-hr (Day 1) QPF guidance from GFS, NAM, ECMWF and the National Weather Service's Hydrometeorological Prediction Center (HPC) for TCs bringing rainfall impact upon continental United States under HPC's advisory responsibility during the 2005-2007 hurricane seasons. It was found that, in general, HPC provided better forecasts than raw model QPF, especially for heavy rain events. Brennan *et al*. (2008) attributed this to more accurate track forecasts and forecasters' experience. Results from locally conducted research might also be a factor for better HPC's value-added QPF.

6.8 Flood forecasting

6.8.1 Hydrological tools and models

One of the life-threatening damages induced by TCs is flooding, which is related to rainfall intensity and distribution, as well as the geographical and hydrological characteristics of the flood plain. However, uncertainty on forecast track, QPF and inadequacy of the precipitation network will adversely affect the accuracy of the rainfall amount and distribution pattern, which in turn, interacting with the topography and environmental flow features in the flood models, will affect the flood forecast.

A pre-requisite for flood plain management is the development of a package of hydrologic and hydraulic simulation tools to simulate the catchment responses to extreme storm events in a river basin. The package of simulation tools should be capable of incorporating the critical characteristics of tides (astronomical spring tides, sea level rises), waves, storm/typhoon surges at the estuarine end of the river. The tool should also be able to reflect the increase of flood peak due to urbanization, and changes in flood discharges and stages associated with various structural and non-structural developments.

Once calibrated, the tools can be used for assessing potential hazards associated with flood events and for evaluating alternative mitigation measures. These simulation models, together with the established flood hazard data (maps, profiles, and flood stages) can then be used to correlate flood discharge, flood stage, flood probability and damages in the flood prone areas. The tools can be readily extended to other flood-prone areas with comparable hydro-geophysical and land-use developmental settings.

Mathematical hydrological models can be used for flood forecasting. Chen (2004) proposed a statistical model for river flood prediction. Predictors in the model included precipitation intensity that could be traced back to a few days, prevailing water level, vegetation and land surface properties, and the presence of river branches and tributaries.

Some of the hydrological models incorporate the use of Geographic Information System (GIS) and digital elevation model (DEM) data, that help "delineating basin boundary, estimating basin area, generating Thiessen Polygons of the raingauge network, calculating areal-mean rainfall, and computing watershed parameters" (Shong 2006). Tang and Xie (2008) employed the Agricultural Non-Point Source Pollution Model (AGNPS) to investigate the hydrological responses in the Tar Pamlico River basin and successfully simulated the peak flow. AGNPS, with watershed hydrology and a water quality model, topography data, and land use and soil type data, could predict surface runoff and sediment yield for flood modeling.

Results from one model can be used as input for triggering another model. This allows different configurations or suites of models to be set up to suit the local environment. For example, hydraulic model results were used in Australia to refine the operational flood hydrological model for generating a variety of flood forecast products, such as temporal and spatial variability of rainfall and runoff (Shong 2006). Hossain (2004) combined rainfall-runoff modules, a hydrodynamic model, and a flood routing model for flood forecasting in Bangladesh.

6.8.2 Operational products

The Global Flood Alert System (GFAS), under the International Flood Network (IFNet; http://www.internationalfloodnetwork.org/index.html) established in March 2003, utilizes satellite-based rainfall for flood forecasting and warning. It provides rainfall maps, text data, and heavy rain information by precipitation probability estimates. E-mail notification service is available for official hydrological services on request.

The International Center for Water Hazard and Risk Management (ICHARM), under the auspices of United Nations Educational, Scientific and Cultural Organization (UNESCO), is operating a comprehensive software package named Integrated Flood Analysis System (IFAS), accessible through http://www.icharm.pwri.go.jp/. IFAS is a tool kit implementing the "GFAS-Streamflow" concept with satellite-based rainfall data for flood runoff analysis and forecasting in developing countries (Yamashiki and Tsujimura, 2009). It consists of five modules: the main module, the rainfall data input module, GIS data input and analysis module, runoff calculation engine module, and calculation results output module (Fukami et al. 2006). The main module is for initiating and managing the various IFAS functions. The rainfall input module handles the satellite-based and ground-based rainfall data. The GIS data input and analysis module facilitates the import of external GIS data, geophysical data analysis and estimation of hydrological model parameters. The runoff calculation engine module enables the selection of different runoff analysis engines, which are either conceptual or mesh-based distributed-parameter hydrologic models. The output module displays results graphically in different ways. As a result, even in poorly-gauged region with insufficient hydrological and geophysical data, IFAS can still produce effective and efficient flood forecasts (Sugiura et al. 2010).

6.8.3 A forecast technique for diagnosing areas of extreme rainfall

Tropical Cyclone Guba tracked south of Port Moresby in November 2007. The Port Moresby TC warning centre issued flood warnings for provinces adjacent to the track but not for the Oro Province which lay some distance from the track. The death toll from the floods in the Oro Province has been put at more than 200. With training, the extreme rainfall region in Oro Province could have been identified from the warm air advection wind profile over the region in conjunction with microwave data. We relayed this information to PNG forecasters and they asked that this diagnostic technique be included in the literature or in the Global Guide for forecasters.

The turning of winds with height, mostly between the 850hPa and 500hPa levels, has been used by forecasters for decades to diagnose likely regions of thermal advection and thus ascent and descent, but due to its roots in geostrophic theory, the diagnostic is generally not applied in the tropics. An exception is the staff at the Severe Weather Section in the Brisbane office of the Australian Bureau of Meteorology. After more than ten years of use, forecasters there have found the anti-cyclonic turning of winds with height to be an important indicator for extreme tropical and sub-tropical rainfall (Bonell and Callaghan 2008; Bonell et al. 2005; Callaghan and Bonell 2005a&b) see also the numerous rainfall event reports at: http://www.bom.gov.au/qld/flood/fld_reports/reports.shtml

Kevin Tory (2015) shows that in a vortex, where the gradient wind balance approximation is valid, warm air advection may also be equated to ascent.

To show the universal application of the diagnostic, we will examine several other major tropical cyclone-related flood events from various tropical regions.

6.8.3.1 Typhoon Bilis

Typhoon Bilis was the second deadliest event in China since 1983 and the deadliest since 1994. Significant damage occurred in Hunan where heavy flooding and mudslides destroyed over

31,000 homes and caused 526 deaths. Most of the damage and fatalities occurred in the village of Zixing. In all, Bilis was responsible for 843 deaths and 208 people reported missing.

The Chenzhou sonde station is very close to Zixing. The heaviest rain in the whole event (24h to 12Z 15 July) was greater than 250mm near Chenzhou and Zixing. From reports, the heavier rain began around 1600UTC 14th, and according to Gao et al. (2009), this rainfall was not forecast very well, with predicted 24-hour totals less than 100mm in the Zixing area.

Chenzhou winds at 00Z 15 July 2006 were 925hPa 330/31knots, 850hPa 345/33knots, 700hPa 010/23knots and 500hPa 050/29knots, which have the warm air advection pattern in the Northern hemisphere of winds turning clockwise with height. We have quantified this to be strong and equivalent to wind profiles producing extreme rainfall in the Queensland (Australia) sub-tropics.

The warm air advection zone generating extreme rainfall has been found to be best shown on 700hPa charts. The analysis in Figure 6.11 uses the 700hPa winds, 850hPa to 500hPa shears and thickness contours from actual observations to depict a warm air advection zone between Changsha through Chenzhou down to near Qing Yang. Figure 6.12 shows the 6-hourly rainfall, and evident is the N to S band of heavy rain through Chenzhou that developed in the warm air advection zone region early on the 15th.

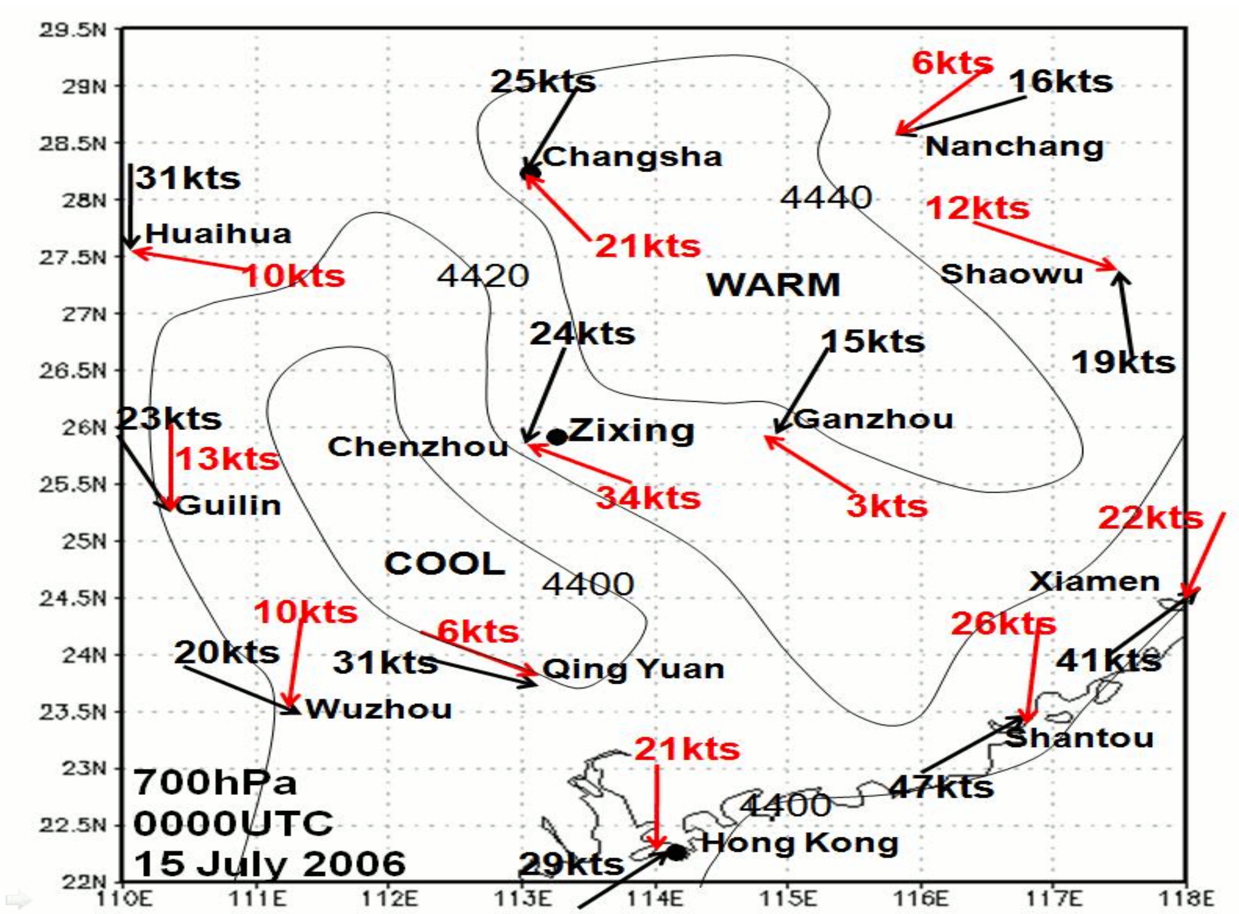

<<Previous

Next>>

Figure 6.11. 700hPa analysis at 0000UTC 15 July 2006 from actual observations. Red arrows 850 to 500hPa shears (knots), black arrows 700hPa winds (knots), and contours 850 to 500hPa thickness (gpm).

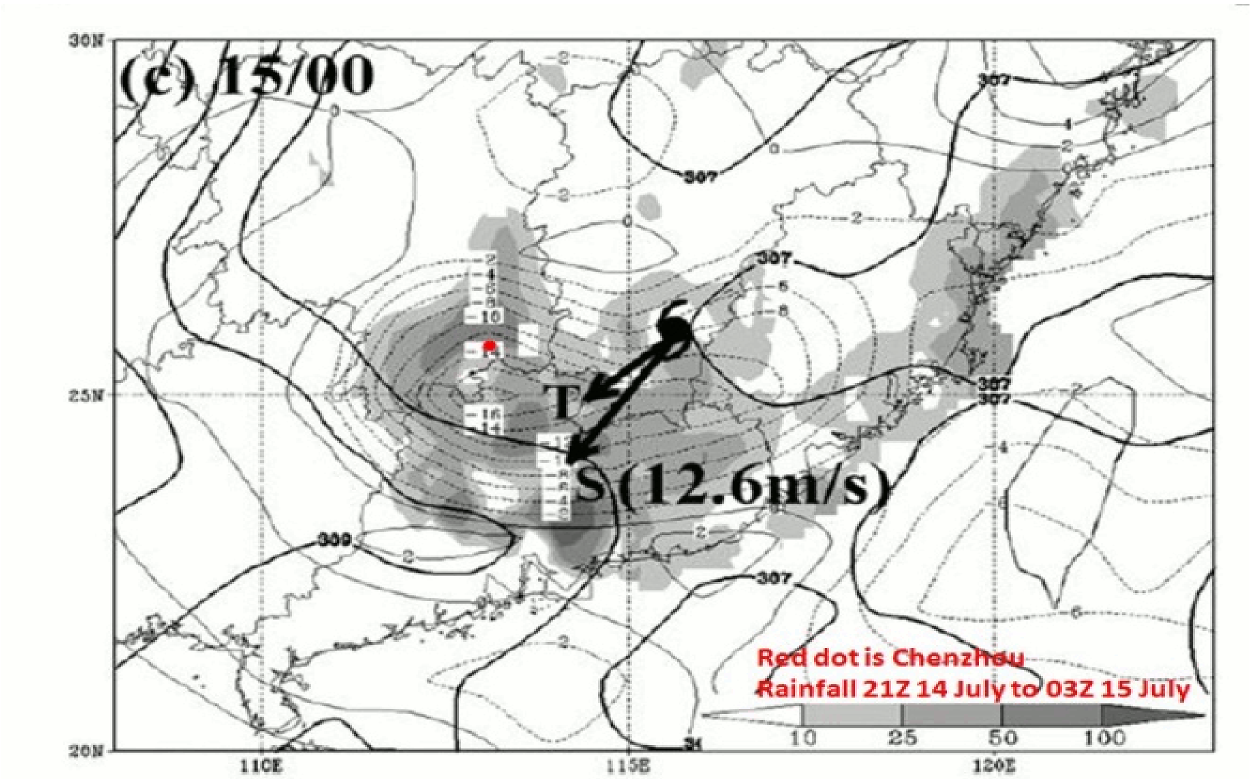

<<Previous

Next>>

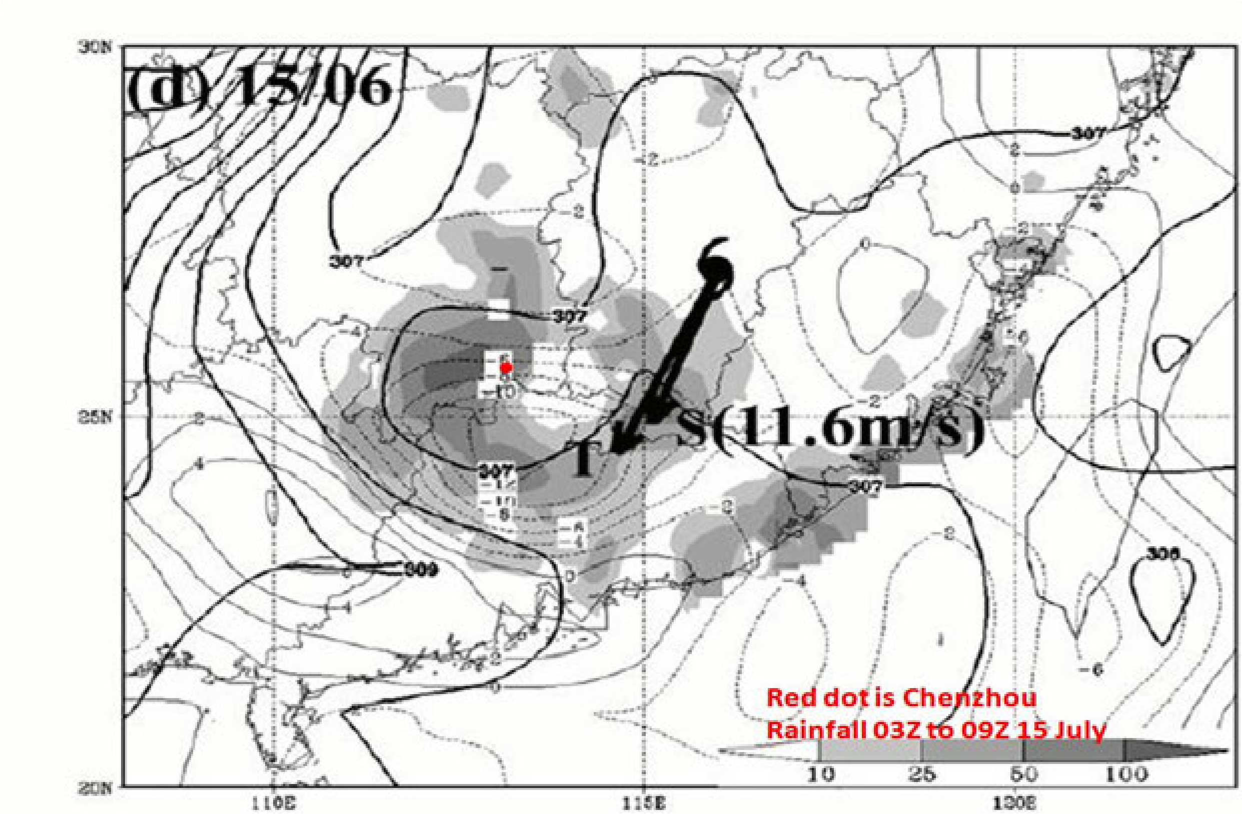

Figure 6.12. Taken from Gao et al. 2009 but focussing on the 6-hourly rainfall near Chenzhou (shown by red dot).

6.8.3.2 Hurricane Mitch

After making landfall as a major hurricane in Honduras, Hurricane Mitch slowly moved over land dropping historic amounts of rainfall in Honduras, Guatemala and Nicaragua with unofficial reports of up to 75 inches (1900 mm). Deaths due to catastrophic flooding made it the second deadliest Atlantic hurricane in history. As of 2008, the official death toll from Mitch was placed at 19,325, with thousands more unaccounted for. Additionally, around 2.7 million people were left homeless as a result of the hurricane.

First, and surprisingly, the highest recorded rainfall over the period from 25 to 31 October 1998 (912 mm) was from Choluteca near the Pacific Coast in Honduras. The maximum 24-hour total there was 467 mm (18.4 in) on 31 October 1998. The highest report from the north coast of Honduras (where landfall occurred and the heaviest totals would normally be expected) was at La Ceiba where 877 mm (34.5 in) was recorded from the 25th to the 31st and 24-hour totals reached 284 mm (11.2 in). Choluteca is close to the Casito Volcano in Nicaragua, which was the scene of a major disaster. Intense, near stationary, rain bands between 0157 UTC 29 October 1998 and 0025 UTC 31 October 1998 produced the exceptional rainfall near the Pacific Coast. In Figure 6.13, we show the microwave imagery with an associated warm air advection pattern at 700hPa, derived from NCEP/NCAR reanalysis data, during the heaviest rainfall. The crater lake atop the dormant volcano filled and parts of the wall collapsed. The resulting massive mud flows covered an area 16 by 8 km (8.6 by 4.3 nmi). At least four villages were totally buried.

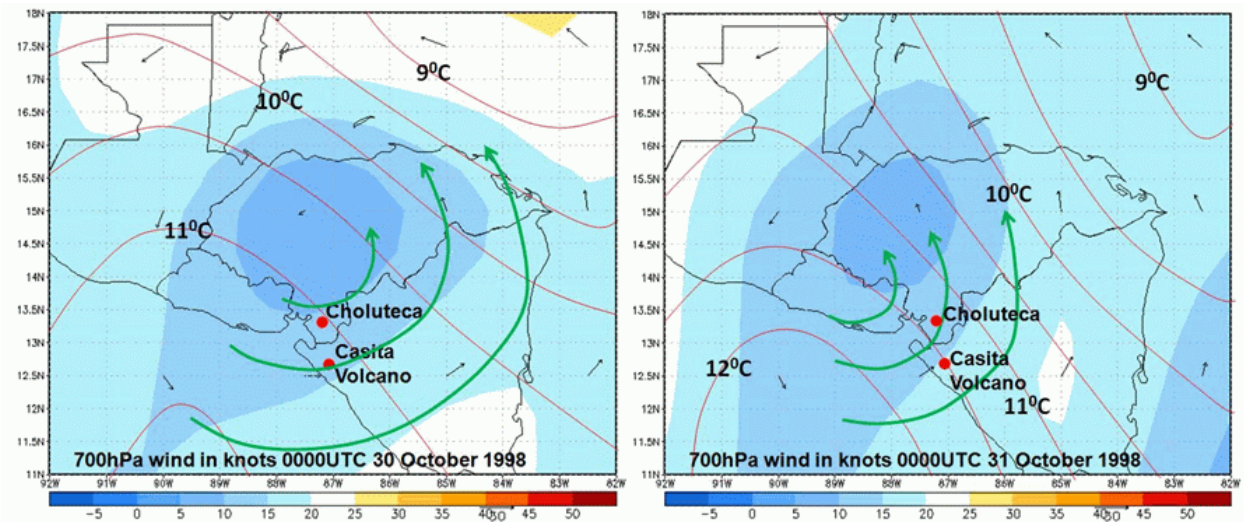

Figure 6.13. The top frames show the stationary heavy rain area near the border of Honduras and Nicaragua from microwave imagery. The lower frames, created from the National Centres for Environmental Prediction/ National Centre for Atmospheric Research (NCEP/NCAR) Reanalysis Project, show the warm air advection (green streamlines) at 700hPa near the border of Honduras and Nicaragua around the same time as the microwave images.

Over 2000 of the dead were from the areas around the volcano. Figure 6.13 shows how the heavy rainfall in the Choluteca and Casito Volcano area was associated with warm air advection at 700hPa.

6.8.3.3 Vietnam floods of November 1999

The floods of November 1999 in Vietnam were the worst in a century, and in total, 793 people lost their lives and 55,000 were made homeless. The floods brought $290 million (US) of damage to the region and caused a further $490 million (US) of economic losses. It is estimated that 1.7 million people in the central Provinces of Vietnam were affected by the floods. From Figure 6.14, the extreme rainfall occurred in a warm air advection region at 700hPa.

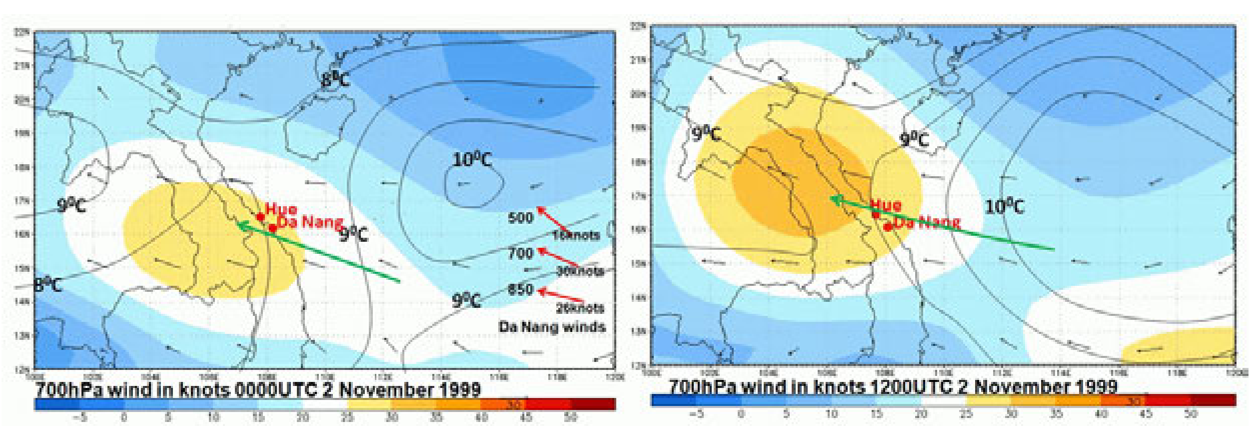

<<Previous Next>>

Figure 6.14. From NCEP/NCAR data the warm air advection at 700hPa through Hue and Da Nang is evident during the extreme rainfall. The clockwise turning with height wind profile at Da Nang at 0000UTC 2 November is also shown.

The rainfall at Hue was **88mm (3.46 in)** in the 24hours to 0000UTC 1 November 1999, **864mm (34.0 in)** in the 24 hours to 2 November 1999, **978mm (38.5 in)** in the 24 hours to 3 November 1999, and **272mm (10.7 in)** in the 24 hours to 4 November 1999.

At Da Nang **93mm (3.66 in)** fell in the 24 hours to 0000UTC 1 November 1999, **126mm (4.96 in)** in the 24 hours to 2 November 1999, and **593mm (23.35 in)** in the 24 hours to 3 November 1999. Da Nang winds showed the warm air advection wind profile during the heaviest rainfall as below:

Da Nang winds 0000UTC 1 November 1999

850hPa 055/18knots

700hPa 085/26knots

500hPa 090/30knots

Da Nang winds 0000UTC 2 November 1999

850hPa 100/26knots 1515.00

700hPa 110/30knots 3155.00

500hPa 135/16knots 5890.00

Da Nang winds 0000UTC 3 November 1999

875hPa 065/18knots

730hPa 090/20knots

633hPa 110/14knots

606hPa 140/14knots

6.8.3.4 Mumbai Floods

A recent example of extreme tropical rainfall occurred when Mumbai (Latitude 19.10N) recorded 944.2mm (37.2 in) in the 24-hour period ending 0330UTC 27 July 2005, which was one of the highest daily totals ever recorded in India. There were 405 fatalities and adding to the chaos apparently was the lack of public information. Radio stations and many television stations claim that they did not receive any weather warnings or alerts by the civic agencies.

The available winds at Mumbai had a warm air advection profile over this period, with strong low level westerly winds veering to north-northwesterly winds at middle levels. This warm air advection profile could easily be seen at the 700 hPa level (Figure 6.15), where northwesterly winds flowed over Mumbai and a strong 700hPa temperature gradient orientated southwest to northeast. Due to icing, the radiosonde balloon at Mumbai only ascended as far as 641hPa.

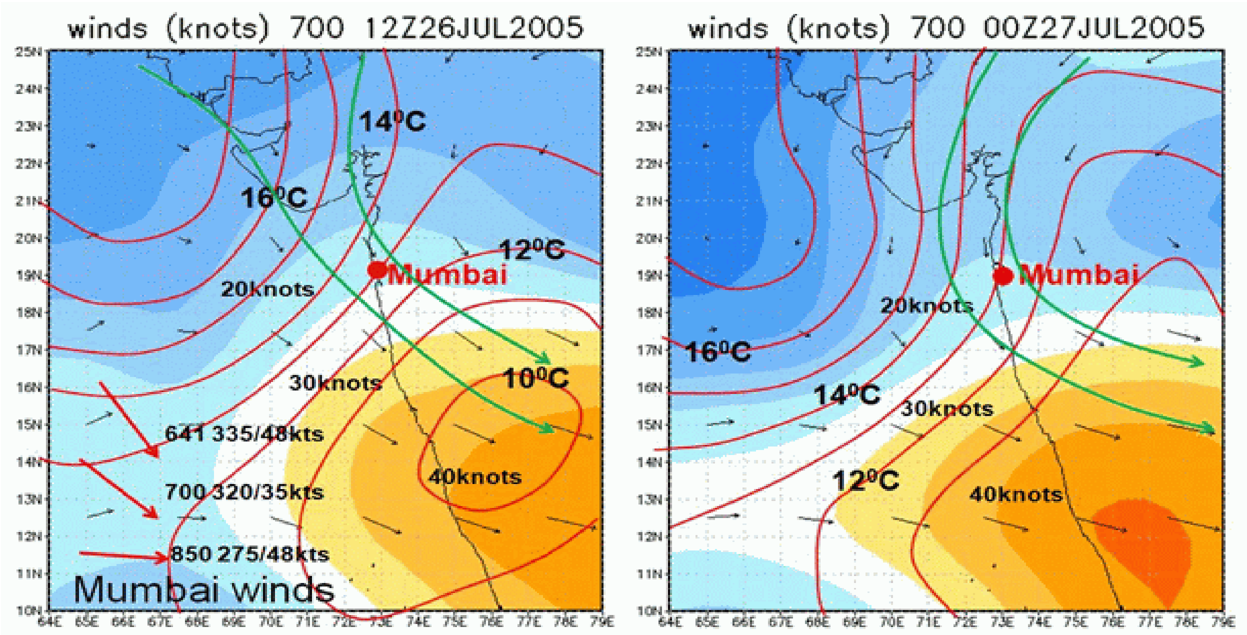

Figure 6.15. From NCEP/NCAR data the warm air advection at 700hPa through Mumbai is evident during the extreme rainfall. The warm air advection wind profile at Mumbai at 1200UTC 26 July 2005 is also shown.

6.8.3.5 Typhoon Chata'an disaster in the Chuuk Lagoon Islands, FSM

Typhoon Chata'an eventually reached super typhoon status; however, its major impact occurred during its early life when it was a tropical storm. The torrential rains of Tropical Storm Chata'an were particularly devastating to the lagoon high islands of Chuuk. A report dated from the Chuuk chapter of the Micronesian Red Cross Society indicated that the death toll was 48 with 73 persons injured. Over 1300 people were left homeless and 130 houses were completely destroyed. Heavy rain unleashed a total of 62 landslides, which caused much of the devastation. Some ranged up to 400-500 metres (1312-1640 ft) in length and were from 200-300 metres (656-984 ft) wide.

Figure 6.16 (top frames) covers the period of heavy rain and shows an area of warm air advection ascent on the western flank of Chata'an, which was aligned with the area of deep convection in the sector of Chata'an (lower frames). Over 500mm of rain was recorded at Chuuk as the area of convection on the western side of the storm passed over the islands. Figure 6.17 shows the clockwise turning with height wind profile at Chuck International airport as the convective complex moved over the island.

<<Previous

Next>>

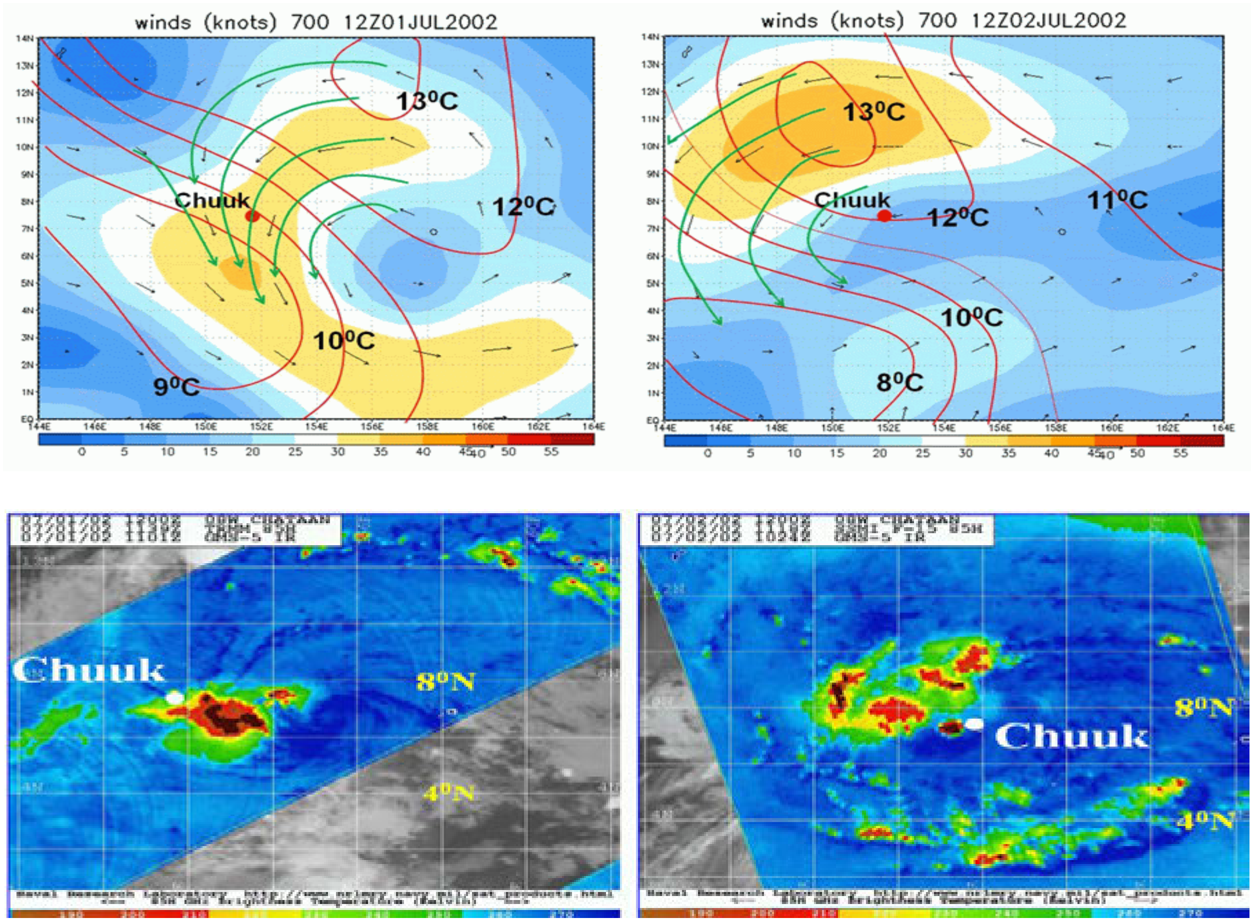

Figure 6.16. NCEP/NCAR 700hPa analysis of warm air advection (top) and corresponding horizontally polarised microwave images at 85GHz for 1139 UTC 1 July 2002 and 1118UTC 2 July 2002.

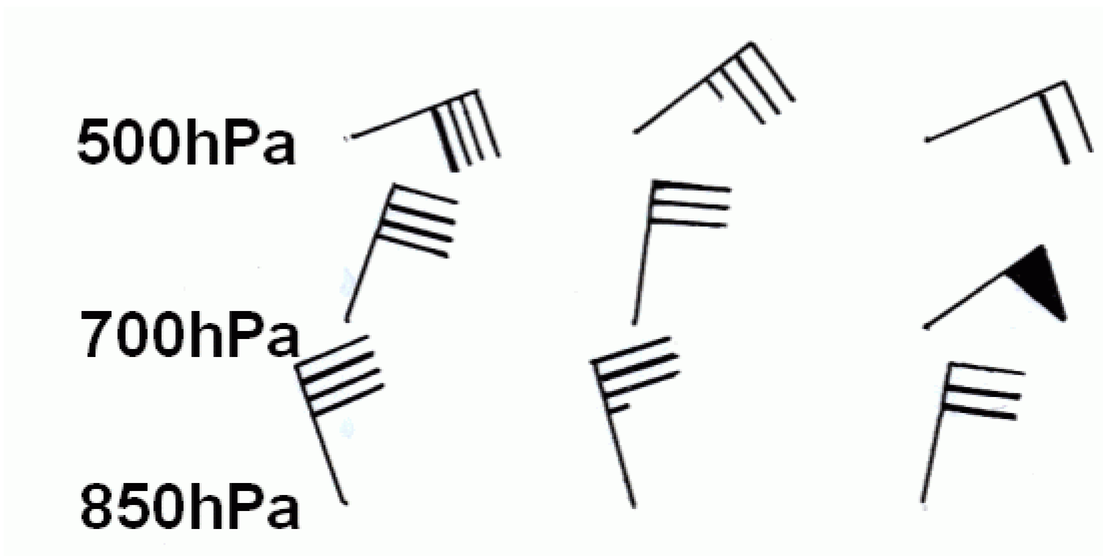

<<Previous Next>>

Figure 6.17. Upper winds at Chuuk Meteorological Office for 0600UTC, 1200UTC and 1800UTC 1 July 2002.

6.8.3.6 World record rainfall La Reunion

Finally, Figure 6.18 illustrates the warm air advection pattern during the world record 6-hourly rainfall event of 688mm (27.1 in) at La Reunion in 1993 (Barceló et al. 1997).

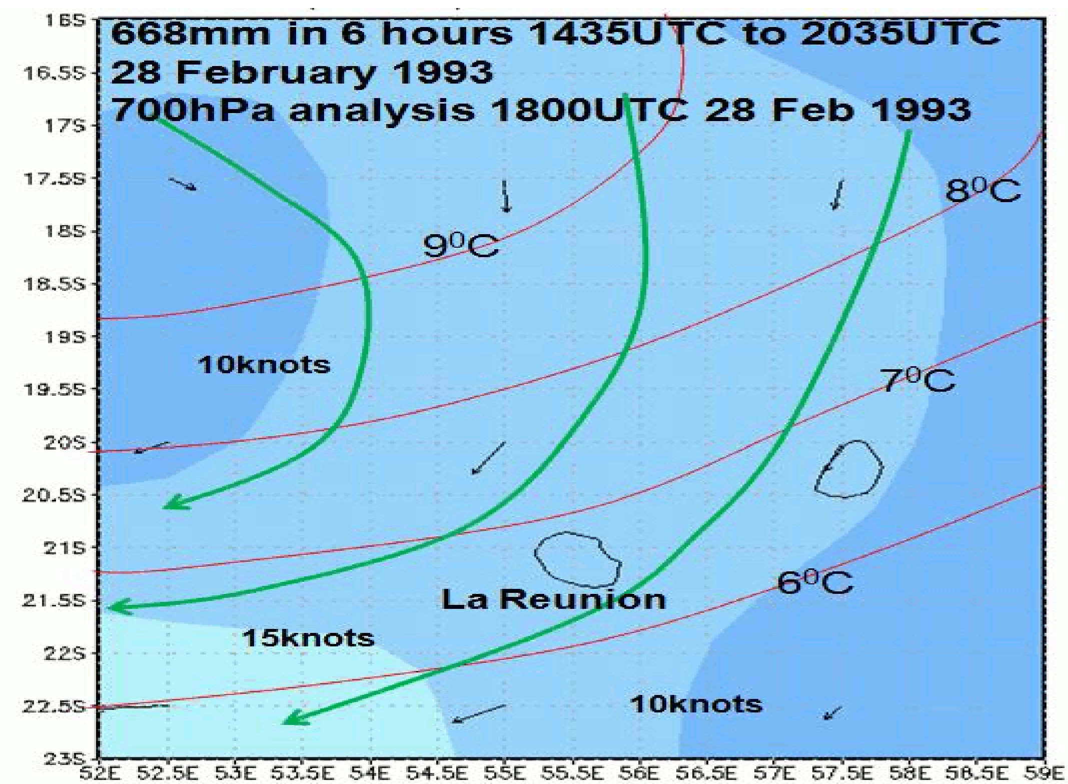

Figure 6.18. NCEP/NCAR 700hPa analysis of warm air advection during world record 6-hourly rainfall at La Reunion in 1993.

6.8.4 Some still pertinent forecast hints from the previous Global Guide

6.8.4.1. Quantitative prediction of tropical cyclone rainfall difficult for four reasons:

1. Rainfall itself is difficult to measure accurately, which hinders both operational analysis of rainfall and the development of improved forecasting aids;
2. Current errors in track prediction mean that accurate rainfall estimates cannot necessarily be transformed into precise predictions, this is especially a problem when a cyclone is moving near regions of significant orography;

3. Interactions between TCs and other weather systems are themselves complicated and poorly understood, so that heavy rain in areas of large-scale ascent and high humidity are difficult to predict;
4. Even within clearly defined threat areas, mesoscale processes, which are poorly understood and difficult to monitor, may determine the distribution of heavy rainfall.

6.8.4.2. Rainfall analysis and forecasting

Because of the meteorological complexity, measurement limitations, and lack of objective aids, analysis and forecasting of heavy rain associated with TCs can at best be indicative of likely outcomes. A suggested mode of operation is to first classify the situation as **uncomplicated** or **complicated**.

1. The TC is relatively well developed;

2. The TC is a day or less from landfall and is moving rapidly enough such that its precipitating region will pass over a given point completely within a day or less;

3. There are no topographic features within the path of the TC, which are significant enough to appreciably alter the rainfall;

4. There are no significant nearby weather systems, including frontal zones, jet streams, or upper-level cut-off lows, which are likely to interact with the TC during its passage inland.

Unfortunately, the majority of forecast situations near landfall involve rapid changes in the character and structure of the precipitation as the system moves inland and interacts with orography and other weather systems. Simple extrapolation procedures will not work very well and the situation is therefore **complicated**. About the best the forecaster can do in advance is to identify a general threat area based on the locations of the TC and surrounding weather systems. The actual locations of heavy rain must then be identified as the event proceeds in order to identify areas, which are accumulating dangerous amounts of rainfall. In the absence of dominating terrain, mesoscale processes such as the development of new convective cells at the merger of old convective outflow boundaries generally determine where within the threat area the heavy rain actually falls. If these mesoscale focusing mechanisms are quasi-stationary, extremely heavy rain may fall even though the convective elements are moving quickly.

6.8.4.3. Determining threat areas

Heavy rain threat areas should be revised at least every 12 hours. Threat areas can change. New threat areas can develop.

The heavy rain threat area for the time (analysis or prognosis) of interest is defined as the intersection of areas defined by surface and 850, 500, and 200 hPa features as listed below:

Satellite: The threat area always includes areas of current heavy convection.

Surface: The upstream edge of the threat area (relative to the surface flow) is one or more of the following: the edge of the coastal plain or beginning of terrain gradient, a frontal boundary, an outflow boundary from previous convection, or the upstream end of a surface convergence zone. The downstream edge is the 15oC isodrosotherm, or a mountain ridge line (beginning of downslope flow).

Tropical Cyclone Track: Add to the threat area the area along the forecast TC track and extending outward to the width of the current central dense overcast (CDO).

850 hPa: The threat area is a corridor 100-200 km (54-108 nmi) on either side of where the low-level jet crosses the surface threat area.

500 hPa: The threat area is beneath and upstream of the upper ridge and bounded to the west by the trough or upper low center.

200 hPa: Threat areas are in regions of jet streak divergence (left-front and right-rear of speed maxima in the northern hemisphere) and streamline diffluence.

The more of the above features present in a region, the greater the threat of heavy rain. The surface features should receive the maximum emphasis.

6.8.4.4. Monitoring the event

Use the rainfall rates every 1-2 hours or as often as imagery or measurements are available. Be especially alert for small, rapidly expanding cells as they typically produce much higher rain rates than large, impressive cloud shields, which are often mostly stratiform. Maintain a single map with positions of active cells from each estimate as this will indicate:

1) where large accumulations are probably occurring, and
2) preferred areas of redevelopment, which in conjunction with surface analyses, can help refine the threat areas.

6.9. References

Adams, I. S., M. H. Bettenhausen, and P. W. Gaiser, 2008: Passive Microwave Remote Sensing of Tropical Cyclones. *28th AMS Conference on Hurricanes and Tropical Meteorology*, Paper 14B.6.

Adler, R. F., and A. J. Negri, 1988: A satellite infrared technique to estimate tropical convective and stratiform rainfall. *J. Appl. Meteorol.*, **27**, 30-51.

Anagnostou, E. N., A. J. Negri, and R. F. Adler, 1999: A satellite infrared technique for diurnal rainfall variability studies. *J. Geophys. Res.*, **104**, 31477-31488.

Atallah, E.H., Bosart, L.F., and Aiyyer, A.R., 2007. Precipitation distribution associated with landfalling tropical cyclones over the eastern United States. *Mon. Weather Rev.* **135**, 2185-2206.

Barceló A., René Robert and Jean Coudray 1997. Major Rainfall Event: The 27 February-5 March 1993 Rains on the Southeastern Slope of Piton de la Fournaise Massif (Reunion Island, Southwest Indian Ocean). *Mon. Wea. Rev*.,**125**, 3341-3346

Bellerby, T., M. Todd, D. Kniveton, and C. Kidd, 2000: Rainfall estimation from a combination of TRMM Precipitation Radar and GOES Multispectral Satellite Imagery through the use of an artificial neural network. *J. Appl. Meteorol.*, **39**, 2115-2128.

Bellon, A., S. Lovejoy, and G. L. Austin, 1980: Combining satellite and radar data for the shortrange forecasting of precipitation. *Mon. Wea. Rev.*, **108**, 1554-1556.

Bonell, M., M. M. Hufschmidt, and J. S. Gladwell (editors), 2005: Hydrology and Water Management in the Humid Tropics: *Hydrological Research Issues and Strategies for Water Management*. Cambridge University Press, Cambridge, UK., 590 pp.

Bonell, M. and J. Callaghan, 2008: The synoptic meteorology of high rainfalls and the storm runoff response in the Wet Tropics, *Living in a Dynamic Tropical Forest Landscape*. N. Stork and S. Turton, Eds. Blackwell Press, 448 pp.

Brakenridge, R, and E. Anderson, 2006: MODIS-based Flood Detection, Mapping and Measurement: The Potential for Operational Hydrological applications. Transboundary Floods: Reducing Risks Through Flood Management, *NATO Science Series: IV: Earth and Environmental Sciences*, **72**, pp. 1-12.

Brennan, M. J., J. L. Clark, and M. Klein, 2008: Verification of Quantitative Precipitation Forecast Guidance from NWP Models and the Hydrometeorlogical Prediction Center for 2005-2007 Tropical Cyclones with Continental U.S. Rainfall Impacts. Poster Session P2H.9, *28th Conference on Hurricanes and Tropical Meteorology, American Meteorological Society*, Orlando, Florida, April 28-May 2.

Buckley, C. D., R. E. Hood, and F. J. LaFontaine, 2009: Application of Airborne Passive Microwave Observations for Monitoring Inland Flooding Caused by Tropical Cyclones. *J. Atmos. Oceanic Technol.*, **26** 2051-2070. doi: http://dx.doi.org/10.1175/2009JTECHA1273.1

Callaghan, J. and M. Bonell 2005a. Synoptic and mesoscale rain producing systems in the humid tropics. *Forests, Water and People in the Humid Tropics International Hydrological Series*, M. Bonell, and L. A. Bruijnzeel, Eds., Cambridge University Press, 925 pp.

Callaghan, J. and M. Bonell 2005b. An overview of the Meteorology and climatology of the humid tropics: *Forests, Water and People in the Humid Tropics International Hydrological Series*, M. Bonell, and L. A. Bruijnzeel, Eds., Cambridge University Press, 925 pp.

Chan, Johnny C. L. and Liang, X, 2003: Convective Asymmetries Associated with Tropical Cyclone Landfall. Part I: f-Plane Simulations. *J. Atmos. Sci.*, **60**, 1560-1576. doi: http://dx.doi.org/10.1175/1520-0469(2003)60<1560:CAAWTC>2.0.CO;2

Chan, S. T., and M.Y. Chan, 2010: applications of Satellite Rain Rate Estimates to the Prediction of Tropical Cyclone Rainfall. *42nd Session of ESCAP/WMO Typhoon Committee*, Singapore, 25-29 January 2010.

Chen, H., 2004: Extended Least Square Algorithm for Nonlinear Stochastic Systems. *ACC2004*, Boston. June 30-July 2, pp. 4758-4763.

Chen, S. S., J. A. Knaff, and F. R. Marks JR., 2006: Effects of Vertical Wind Shear and Storm Motion on Tropical Cyclone Rainfall Asymmetries Deduced from TRMM. *Mon. Wea. Rev.*, **134**, 3191-3208.

Cerveny, R. S., and L. E. Newman, 2000: Climatological Relationships between Tropical Cyclones and Rainfall. *Mon. Wea. Rev.*, **128**, 3329-3336. doi: http://dx.doi.org/10.1175/1520-0493(2000)128<3329:CRBTCA>2.0.CO;2

Cheung, K. K. W., L.-R. Huang, and C.-S. Lee, 2008: Characteristics of rainfall during tropical cyclone periods in Taiwan. *Nat. Hazards Earth Syst. Sci*.,**8**, 1463-1474. http://www.nat-hazards-earth-syst-sci.net/8/1463/2008/nhess-8-1463-2008.html doi:10.5194/nhess-8-1463-2008.

Ebert, E., A.E. Salemi, M. Turk, M. Spampata, S. Kusselson, 2009: Validation of the ensemble tropical rainfall Potential (e-TRaP) for landfalling tropical cyclones. *16th Conference on Satellite Meteorology and Oceanography*, AMS 89th Annual Meeting, Phoenix, AZ, 12-15 January 2009.

El-Nimri, S., S. AlSweiss, W. L. Jones, J. Johnson, and E. Uhlhorn, 2008: Hurricane Imaging Radiometer Wide Swath Simulation for Wind Speed and Rain Rate, *Proc. IEEE IGARSS-08*, Jul. 6 - 11, 2008, Boston, MA.
Also see: El-Nimri, Salem F., W. Linwood Jones, Eric Uhlhorn, Christopher Ruf, James Johnson, and Peter Black, An Improved C-Band Ocean Surface Emissivity Model at Hurricane-Force Wind Speeds over a Wide Range of Earth Incidence Angles, *IEEE Geosci. & Remote Sens. Letters*, **7 (4)**, pp. 641-645, Oct 2010.

Ferraro, R., P. Pellegrino, M. Turk, W. Chen, S. Qiu, R. Kuligowski, S. Kusselson, A. Irving, S. Kidder, and J. Knaff, 2005: The Tropical Rainfall Potential (TRaP) Technique. Part II: Validation. *Wea. Forecasting*, **20**, 465-475.

Fukami, K., N. Fujiwara, N. Fujiwara, M. Ishikawa, M. Kitano, T. Kitamura, T. Shimizu, S. Hironaka, S. Nakamura, T. Goto, M. Nagai, and S. Tomita, 2006: Development of an integrated flood runoff analysis system for poorly-gauged basins. *7th International Conference on Hydroinformatics (HIC)*, Nice, France, September 2006.

Gao, S., Z. Meng, F. Zhang, and L. F. Bosart, 2009: Observational analysis of heavy rainfall mechanisms associated with severe Tropical Storm Bilis (2006) after its landfall. *Mon. Wea. Rev.*, **137**, 1881-1897.

Griffith, C. G., W. L. Woodley, P. G. Grube, D. W. Martin, J. Stout, and D. N. Sikdar, 1978: Rainestimation from geosynchronous satellite imagery - Visible and infrared studies. *Mon. Wea. Rev.*, **106**, 1153-1171.

Grody, N. C., 1984: Precipitation monitoring over land from satellites by microwave radiometry. *Proc. IGARSS' 84 Symposium*, Strasbourg, 27-30 August.

Grody, N. C., F. Weng, and R. R. Ferraro, 1999: Application of AMSU for obtaining hydrological parameters. *Microwave Radiometry and Remote Sensing of the Environment*, P. Pampaloni and S. Paloscia Ed., VSP Int. Sci. Publisher, Utrecht (The Netherlands), 339-351.

Gruber, A.,1973: Estimating rainfall in regions of active convection. *J. Appl. Meteorol.*, **12**, 110-118.

Haddad, Z., E. A. Smith, C. D. Kummerow, T. Iguchi, M. Farrar, S. Darden, M. Alves, and W. Olson, 1997: The TRMM 'Day-1' radar/radiometer combined rain-profile algorithm. *J. Meteor. Soc. Japan*, **75**, 799-808.

Harville, S. L., 2009: Effects of Appalachian topography on precipitation from landfalling hurricanes.*MS thesis, North Carolina State University*, 320pp. (Available from http://repository.lib.ncsu.edu/ir/handle/1840.16/2849)

Hood, R. E., R. Atlas, P. Black, S. S. Chen, C. C. Hennon, J. W. Johnson, L. Jones, T. L. Miller, C. S. Ruf, and E. W. Uhlhorn, 2008: An overview of the Hurricane Imaging Radiometer (HIRAD). *28th AMS Conference on Hurricanes and Tropical Meteorology*, April 28 - May 2, 2008, Orlando, FL. Also see: Hood, R. Amarin, M. Bailey, P. Black, M. James, J. Johnson, L. Jones, B. Lim, C. Ruf, K. Stephens, and V. Rohwedder, 2007: Development of the Hurricane Imaging Radiometer (HIRAD) Using a Systems Engineering Approach. *61st Interdepartmental Hurricane Conference*, March 5-9, 2007, New Orleans, LA.

Hossain, A.N.H. Akhtar, 2004: Flood Management: Issues and Options. Presented in the *International Conference organized by the Institute of Engineers*, Bangladesh.

Hsu, K., X. G. Gao, S. Sorooshian, and H. V. Gupta, 1997: Precipitation estimation from remotely sensed information using artificial neural networks. *J. Appl. Meteor.*, **36**, 1176-1190.

Iguchi, T., T. Kozu, R. Meneghini, J. Awaka, and K. Okamoto, 2000: Rain-profiling algorithm for the TRMM precipitation radar. *J. Appl. Meteorol.*, **39**, 2038-2052.

Jiang, H., G. Feingold, and W. R. Cotton (2002), Simulations of aerosol-cloud-dynamical feedbacks resulting from entrainment of aerosol into the marine boundary layer during the Atlantic Stratocumulus Transition Experiment, *J. Geophys. Res.*, **107(D24)**, 4813.

Jiang, H., P. G. Black, E. J. Zipser, F. D. Marks Jr., and E. W. Uhlhorn, 2006: Validation of Rain-Rate Estimation in Hurricanes from the Stepped Frequency Microwave Radiometer: Algorithm Correction and Error Analysis. *J. Atmos. Sci.*, **63**, 252-267. doi: http://dx.doi.org/10.1175/JAS3605.1
Also see: Jiang, J. H., B. Wang, K. Goya, K. Hocke, S. F. Eckermann, J. Ma, D. L. Wu, and W. G. Read, 2004: Geographical distribution and interseasonal variability of tropical deep convection: UARS MLS observations and analyses. *J. Geophys. Res.*, **109**.D03111, doi:10.1029/2003JD003756.

Jiang, H., and E. J. Zipser, 2010: Contribution of Tropical Cyclones to the Global Precipitation from Eight Seasons of TRMM Data: Regional, Seasonal, and Interannual Variations. *J. Climate*, **23**, 1526-1543. doi: http://dx.doi.org/10.1175/2009JCLI3303.1

Joyce, R. J., J. E. Janowiak, P. A. Arkin, and P. Xie, 2004: CMORPH: A method that produces global precipitation estimates from passive microwave and infrared data at high spatial and temporal resolution, *J. Hydrometeorol.*, **5**, 487-503.

Kidd, C., 1998: On rainfall retrieval using polarization-corrected temperatures. *Int. J. Remote Sensing*, **19**, 981-996.

Kidder, S. Q., J. A. Knaff, S. J. Kusselson, M. Turk, R. R. Ferraro, and R. J. Kuligowski, 2005: The tropical rainfall potential (TRaP) technique. Part I: Description and examples. *Wea. Forecasting*, **20**, 456-464.

Krishnamurti, T. N., T. N., A. K. Mishra, A. Chakraborty, and M. Rajeevan, 2009a: Improving global model precipitation forecasts over India using downscaling and the FSU superensemble. Part I: 1-5-day forecasts. *Mon. Wea. Rev.*, **137**, 2713-2735.

Krishnamurti, T. N., A. D. Sagadevan, A. Chakraborty, A. K. Mishra, A. Simon, 2009b: Improving multimodel weather forecast of monsoon rain over China using FSU superensemble. *Advances in Atmospheric Sciences*, **26**, pp 813-839.

Lai, E. S. T., and W. K. Wong, 2006: Quantitative Precipitation Nowcast of Tropical Cyclone Rainbands Case Evaluation in 2006. Hong Kong Observatory.

Lambrigtsen, B., T. Gaier, P. Kangaslahti, and A. Tanner, 2008: A Geostationary Microwave Sounder for NASA and NOAA. Jet Propulsion Laboratory, California Institute of Technology. https://cimss.ssec.wisc.edu/itwg/itsc/itsc16/proceedings/B31_Lambrigtsen.pdf

Levizzani,V., R. Amorati, and F. Meneguzzo, 2002: A Review of Satellite-based Rainfall Estimation Methods. MUltiple-Sensor Precipitation Measurements, Integration, Calibration and Flood Forecasting (MUSIC) Project. EVK1-CT-2000-00058 Deliverable 6.1 04/02/2002.

Li, P.W., W.K. Wong, K.Y. Chan, and Edwin S.T. Lai, 2000: SWIRLS - An Evolving Nowcasting System.*Hong Kong Observatory Technical Note, No.100*.

Li, P. W., and E. S. T. Lai, 2004: Short-range quantitative precipitation forecasting in Hong Kong, *J. Hydrology*, **288**, 189-209.

Lonfat, M., F. D. Marks, and S. S. Chen, 2004: Precipitation Distribution in Tropical Cyclones Using the Tropical Rainfall Measuring Mission (TRMM) Microwave Imager: A Global Perspective. *Mon. Wea. Rev.*, **132**, 1645-1660.

Lonfat, M., R. Rogers, T. Marchok, and F. D. Marks, Jr., 2007: A parametric model for predicting hurricane rainfall. *Mon. Weather Rev.*, **135**, 3086- 3097. doi:10.1175/MWR3433.1.

Lovejoy, S., and G. L. Austin, 1979: The delineation of rain areas from visible and IR satellite data from GATE and mid-latitudes. *Atmos.-Ocean*, **17**, 77-92.

Marchok, T., R. Rogers, and R. Tuleya, 2007: Validation schemes for tropical cyclone quantitative precipitation forecasts: Evaluation of operational models for US landfalling cases. *Wea. Forecasting*, **22**. DOI: 10.1175/WAF1024.1

Marks, F. D., G. Kappler, and M. DeMaria, 2002: Development of a Tropical Cyclone Rainfall Climatology and Persistence (R-CLIPER) Model. Reprints of the *25th Conference on Hurricanes and Tropical Meteorology*, AMS, San Diego, CA.

Marks, F. D., 2003: State of the Science: Radar View of Tropical Cyclones. *Meteorological Monographs*, **30**.

Medlin, J. M., S. K. Kimball, and K. G. Blackwell, 2007: Radar and rain gauge analysis of the extreme rainfall during hurricane Danny's (1997) landfall. *Mon. Wea. Rev.*, **135**, 1869-1888.

Miller, S. W., P. A. Arkin, and R. J. Joyce, 2000: A combined microwave/infrared rain rate algorithm.*Int. J. Remote Sens.*, **22**, 3285-3307.

Mishra, A. K., and T. N. Krishnamurti, 2007: Current status of multimodel Superensemble and operational NWP forecast of the Indian summer monsoon. *Journal of Earth System Science*, **116(5)**, 369-384.

Negri, A. J., R. F. Adler, and P. J. Wetzel, 1984: Rain estimation from satellite: An examination of the Griffith-Woodley technique. *J. Climate Appl. Meteorol.*, **23**, 102-116.

Porcù, F., M. Borga, and F. Prodi, 1999: Rainfall estimation by combining radar and infrared satellite data for nowcasting purposes. *Meteorol. Appl.*, **6**, 289-300.

Quinlan, K. R., 2008: Conditions influencing Hurricane Emily's (2005) precipitation patterns, convection, and upper tropospheric outflow. *M.S. thesis, Department of Atmospheric Science, University of Alabama in Huntsville*, 116 pp.

Randall S. Cerveny and Lynn E. Newman, 2000: Climatological Relationships between Tropical Cyclones and Rainfall. *Mon. Wea. Rev.*, **128**, 3329–3336.

Ritchie, E. A., and D. Szenasi, 2006: The Impact of Tropical Cyclone Remnants on the Rainfall of the North American Southwest Region. Preprints, *27th Conf. on Hurricanes and Tropical Meteorology* P2.4, Monterey, CA. Amer. Meteor. Soc.

Rodgers, E. B., R. F. Adler, and H. F. Pierce, 2000: Contribution of tropical cyclones to the North Pacific climatological rainfall as observed from satellites. *J. Appl. Meteor.*, **39**, 1658-1678.

Rodgers, E. B., R. F. Adler, and H. F. Pierce, 2001: Contribution of Tropical Cyclones to the North Atlantic Climatological Rainfall as Observed from Satellites. *J. Appl. Meteor.*, **40**, 1785-1800. doi: http://dx.doi.org/10.1175/1520-0450(2001)040<1785:COTCTT>2.0.CO;2

Sandholt, I., L. Nyborg, B. Fog, M. Lô, O. Bocoum, and K. Rasmussen, 2003: Remote sensing techniques for flood monitoring in the Senegal River Valley, *Danish Journal of Geography*, **103 (1)**, 71-81.

Shong, 2006: Shuanzhu Gao, Zhiyong Meng, Fuqing Zhang and Lance F. Bosart, 2009: Observational Analysis of Heavy Rainfall Mechanisms Associated with Severe Tropical Storm Bilis (2006) after its Landfall. *Mon. Wea. Rev.*, **137**, 1881-1897.

Smith, R. K., M. T. Montgomery, and S. Vogt, 2008: A critique of Emanuel's hurricane model and potential intensity theory. *Q. J. R. Meteorol. Soc.*, **134**, 551-561.

Smith, R. B., P. Schafer, D. Kirshbaum, and E. Regina, 2009: Orographic Enhancement of Precipitation inside Hurricane Dean. *J. Hydrometeor*, **10**, 820-831. doi: http://dx.doi.org/10.1175/2008JHM1057.1

Sorooshian, S., K.-L. Hsu, X. Gao, H. V. Gupta, B. Imam, and D. Braithwaite, 2000: Evaluation of PERSIANN system satellite–based estimates of tropical rainfall. *Bull. Am. Meteor. Soc.*,**81**, 2035–2046.

Sugiura, T., Fukami, K., Fujiwara N., Hamaguchi, K., Nakamura, S., Hironaka, S., Nakamura, K., Wada, T., Ishikawa, M., Shimizu, T., Inomata, H., Itou, Z., 2010 (2009 in text): "Experimental application of flood forecasting system (IFAS) using satellite-based rainfall." *Ninth International Conference on Hydroingormatics*. Tianjin, China: HIC2010. 1786-1793. Also see: Sugiura, A., S. Fujioka, S. Nabesaka, T. Sayama, Y. Iwami, K. Fukami, S. Tanaka and K.Takeuchi, 2013: Challenges on modelling a large river basin with scarce data: A case study of the Indus upper catchment. *20th International Congress on Modelling and Simulation*, Adelaide, Australia, 1-6 December 2013. http://www.mssanz.org.au/modsim2013

Tang, Q., and L. Xie, 2008: Modelling inland flooding due to tropical cyclones. *28th Conference on Hurricanes and Tropical Meteorology, American Meteorological Society*, Orlando, Florida, April 28-May 2, 2008.

Todd, M. C., C. Kidd, D. Kniveton, and T. J. Bellerby, 2001: A combined satellite infrared and passive microwave technique for estimation of small-scale rainfall. *J. Atmos. Oceanic Technol.*, **18**, 742-755.

Tory, K., 2015: (in press). *Australian Meteorological and Oceanographic Journal*

Tuleya, R. E., M. DeMaria, and R. J. Kuligowski (2007): Evaluation of GFDL and simple statistical model rainfall forecasts for U.S. landfalling tropical storms. *Wea. Forecasting,* **22**, 56-70

Turk, F. J., F. S. Marzano, and E. A. Smith, 1998: Combining geostationary and SSM/I data for rapid rain rate estimation and accumulation. Prepr. *9th Conf. Satellite Meteorology and Oceanography*, AMS, 462-465.

Turk, F. J., J. Hawkins, E. A. Smith, F. S. Marzano, A. Mugnai, and V. Levizzani, 2000: Combining SSM/I, TRMM and infrared geostationary satellite data in a near-realtime fashion for rapid precipitation updates: advantages and limitations. *Proc. The 2000 EUMETSAT Meteorological Satellite Data Users' Conference*, 452-459

Vicente, G. A., and R. A. Scofield, 1996: Experimental GOES-8/9 derived rainfall estimates for flash flood and hydrological applications. *Proc. The 1996 EUMETSAT Meteorological Satellite Data Users' Conf.*, EUMETSAT, 89-96.

Wang, Y., Y. Wang, and H. Fudeyasu, 2009: The Role of Typhoon Songda (2004) in Producing Distantly Located Heavy Rainfall in Japan. *Mon. Wea. Rev.,* **137**, 3699-3715.

Wu, C.-C., K. K. W. Cheung, and Y.-Y. Lo, 2009: Numerical study of the rainfall event due to the interaction of Typhoon Babs (1998) and the northeasterly monsoon, *Mon. Weather Rev.,* **137**, 2049-2064, doi:10.1175/2009MWR2757.1.

Wylie, D. P., 1979: An application of a geostationary satellite rain estimation technique to an extra-tropical area. *J. Appl. Meteorol.*, **18**, 1640-1648.

Yamashiki, Y., Tsujimura, M., 2009: Special Issue: Japan Society of Hydrology and Water Resources - Annual Issue VIII. *Hydrological Processes,* **23 (4)**, pp. 523-647. ISSN0885-6087 DOI10.1002/hyp.7181.

Yokoyama, C., and Y. N. Takayabu, 2008: A statistical study on rain characteristics of tropical cyclones using TRMM satellite data. *Mon. Wea. Rev.,* **136**, 3848-3862.